Space-based Aperture Array For Ultra-Long Wavelength Radio Astronomy

Raj Thilak Rajan Albert-Jan Boonstra Mark Bentum Marc Klein-Wolt
Frederik Belien Michel Arts Noah Saks Alle-Jan van der Veen

December 18, 2019

Abstract

The past decade has seen the advent of various radio astronomy arrays, especially for low-frequency observations below 100MHz. These developments have been driven by interesting and fundamental scientific questions, such as the study of the dark ages and the epoch of re-ionization, which can be achieved by detecting the highly red-shifted 21cm line emission, observable at frequencies below 30MHz. However, Earth-based radio astronomy observations at these frequencies are severely restricted due to man-made interference, ionospheric distortion, and almost complete non-transparency of the ionosphere below 10MHz. Therefore, this narrow spectral band of $0.3 - 30$MHz remains one of the last unexplored frequency range in radio astronomy. A straightforward solution to observe at these frequencies is to deploy a space-based antenna array comprising of numerous satellites, which would synthesize a large aperture at these wavelengths. In the past, such space-based radio astronomy missions were principally limited by technology and computational resources, however current technology and processing trends indicate otherwise. Furthermore, previously successful single-satellite missions, such as the lunar orbiter RAE-2 (Radio astronomy explorer 2), were restricted by very poor spatial resolution. However, recently concluded studies, such as DARIS (Distributed Aperture Array for Radio Astronomy In Space) have shown the feasibility of a 9 satellite constellation using off the shelf components, which offer significant improvement in resolution and sensitivity. The aim of this article is to discuss the current trends and technologies towards the feasibility of a space-based aperture array for astronomical observations in the Ultra-Long Wavelength (ULW) regime of greater than 10m i.e., below 30MHz. We briefly present the achievable science cases, and discuss the system design for selected scenarios such as extra-galactic surveys. An extensive discussion is presented on various sub-systems of the potential satellite array, such as radio astronomical antenna design, the on-board signal processing, communication architectures, and joint position-time estimation of the satellite network. In view of a scalable array, and to avert single point of failure, we present distributed solutions for the ULW space-based array. We highlight the benefits of the potential deployment locations, and summarize the technological challenges for future space-based radio arrays.

Cite this article as:
Raj Thilak Rajan, Albert-Jan Boonstra, Mark Bentum, Marc Klein-Wolt, Frederik Belien, Michel Arts, Noah Saks, and Alle-Jan van der Veen. "Space-based aperture array for ultra-long wavelength radio astronomy." Experimental Astronomy 41, no. 1-2 (2016): 271-306. https://doi.org/10.1007/s10686-015-9486-6

1 Introduction

The success of Earth-based radio astronomy in the frequencies between 30MHz and 3GHz is jointly credited to the Earth's transparent ionosphere, and to the steady technological advancements during the past decades. In recent times, radio astronomy has seen the advent of a large suite of radio telescopes, particularly towards the longer observational wavelengths, i.e., $\geq$ 3m. These arrays include the Murchison widefield array (MWA) (47), Low frequency array (LOFAR) (74) and the Long wavelength array (LWA) (27) to name a few. However, Earth-based astronomical observations at these ultra-long wavelengths are severely restricted due to various reasons (37). For instance, due to ionospheric distortion especially during the solar maximum period, when scintillation occurs, the celestial signals suffer from de-correlation among the elements of a ground based telescope array (39). Currently, advanced calibration and mitigation techniques are employed in the LOFAR telescope array, which can be used to remove these distortions, provided the time scale of disturbances is much longer than the time needed for calibration (77). Furthermore, at frequencies below 10MHz the ionosphere is completely non-transparent, which impede observations by ground-based instruments. In addition to ionospheric interference, man-made transmitter signals below 30MHz also impede terrestrial based astronomical observations. This man-made terrestrial interference was even observed as far as $\sim 400,000$km away from Earth by lunar orbiters, despite being limited by poor resolution (3). Due to the above mentioned reasons, the very low frequency range of $0.3 - 30$ MHz remains one of the last unexplored frontier in astronomy. An unequivocal solution to observe the radio sky at ULW with the desired resolution and sensitivity is to deploy a dedicated satellite array in outer-space. Such a space-based array must be deployed sufficiently far away from Earths' ionosphere, to avoid terrestrial interference, and offer stable conditions for calibration during scientific observations.

1.1 Science at ultra-long wavelengths

A space-based aperture array for the virtually unexplored ULW, would address a wealth of science cases, which would undoubtedly lead to novel scientific discoveries, similar to the unveiling of other wavelength domains in the past. For many of these science cases, such an array would offer additional information to the existing maps at radio, optical, infrared, sub-mm or high frequency X-ray or gamma-ray wavelengths, and thereby provide insight into the processes that take place at the lowest energies and the largest physical scales. These science cases include the study of (extra) galactic surveys, exploring our solar system neighbourhood, and observing transients such as (extra) solar and planetary bursts, and the study of high energy particle physics (34; 41). Other key science cases include the study of large-scale galaxy clusters, radio galaxies, and the detection of Jupiter-like flares, and Crab-like pulses from (extra) galactic sources (79).

The greatest advance in science is expected from the study of the very early universe, in a period referred to as the cosmological dark ages (62). The dark ages is the period between the epoch of recombination (378,000 years after big bang) when the universe became transparent, and the epoch of reionisation (EoR) when the first stars and galaxies started to reionise the neutral hydrogen. The global 21-cm wave absorption signature from the primordial hydrogen in the dark ages at z=50 is expected to peak around 30MHz. In principle, a single antenna placed at an ideal location on the moon (i.e. under low RFI and stable temperature and gain conditions), is sufficient to detect the global dark ages signal at a 5σ level with one year of integration time period (34). However, in order to trace the spatial variations of hydrogen at arcsecond or even arcminute scale resolution, a larger sensitivity, and thus a larger collecting area is required. For instance up to 105 individual antenna elements synthesizing and aperture

of 0.5km^2 would acheived a spatial resolution of $10'$ (45). Therefore, in addition to a low-RFI, low-temperature and stable gain location, a ULW radio interferometer that aims at detecting the arcmin variations in the mass distribution of the dark ages and the EoR, must have a large collecting area (in the order of few km^2). The ideal deployment locations for such an array include the farside of the moon, an eternally dark crater on the lunar south or north pole, the Heliocentric Earth leading/trailing orbits, Sun-Earth L2 point, or the Lunar orbits.

1.2 Previous studies

The proposition for a space-based radio astronomy instrument is not novel (76; 9; 10; 37). One of the first such proposals was made by Gorgolewski in 1965 (29), who discussed the benefits of a moon-based radio interferometer. In 1968 and 1973, two radio astronomy explorers (RAEs) were launched, namely the RAE-1 (75) and RAE-2 (3) respectively. The RAE-1 covered a frequency range of 0.2MHz to 9.2MHz using two 229 meter V-antennas and one 37 meter electric dipole, while the RAE-2 mapped the non-thermal galactic emission in the frequency range of 25kHz to 13MHz using a single 37m dipole antenna, achieving a resolution of $37°$. Despite their poor resolution, these single-satellite explorers were the first dedicated space missions exclusively for ULW radio astronomy.

Science at the ultra-long wavelengths was revived in the 1990s with a particular focus on Lunar based arrays (21; 23). The Lunar surface on the far-side presents a large and stable platform for antennas and shields unwanted interference from the Earth and the Sun (78; 43; 69; 5), which motivated studies such as Very low frequency array (VLFA) (66), Moon-based epoch of reionization imaging telescope (MERIT) (36) and more recently the Dark ages explorer (DEX) (42). Along similar lines, lunar orbiting single-satellite missions dedicated for radio astronomy such as LORAE (22) and DARE (24) were also investigated, to map bright sources and to facilitate relatively easier Earth-based down-link of science data. Furthermore, the pursuit of higher angular resolutions has led to Earth-orbiting single-satellite missions such as Highly advanced laboratory for communications and astronomy (HALCA) (32), and Radio Astron (38) which enable Earth-space very long baseline interferometry (31).

In contrast to these lunar arrays and single-satellite missions, the concept of space-based ULW array for radio astronomy has received considerably less attention in the past decades, which is our primary focus in this article. The successful single-satellite RAE missions motivated the first space-based array proposal to NASA i.e., the Low Frequency Space Array (LFSA) (76). Another notable NASA funded study in this regard was the Astronomical low frequency array (ALFA) concept, which proposed an array of $10 - 16$ satellites in a distant retrograde orbit (35). More recently, two ESA funded studies namely Formation-flying sub-Ionospheric Radio astronomy Science and Technology (FIRST) (12) and the Distributed aperture array for radio astronomy in space (DARIS) (15), investigated passive-formation flying missions for space-based satellite arrays (see Table 1). The FIRST study proposed a constellation of 7 satellites deployed at the second Earth-Moon Lagrange (L2) point, sufficiently far enough from Earth to avert interference and allowed for a low-drift orbit. On the other hand, the DARIS study primarily investigated the feasible ULW science cases and showed ready feasibility of 9 satellites using existing off the shelf technologies. The benefits of both these studies were combined in the SURO mission, which aims to deploy an array in the Sun-Earth L2 Lagrange point. In all these studies, a dedicated centralized mothership managed the processing, communication and downlink to Earth. However, futuristic arrays with a larger number of satellites (e.g., ≥ 10), such as Orbiting low frequency antennas for radio astronomy (OLFAR) (11; 59), will operate cooperatively and employ distributed architectures for processing, communication and Earth downlink, to avoid single point of failure and for efficiency.

	FIRST	**DARIS**	**SURO-LC**	**OLFAR**
Timeline	$2009-2010$	$2009-2010$	$2011-2012$	$2010-2014$
No. of satellites (N)	$6^{\dagger}+1^{\ddagger}$	$8^{\dagger}+1^{\ddagger}$	$\geq 8^{\dagger}+1^{\ddagger}$	≥ 10
No. of polarizations (N_{pol})	3	3	3	3
Obs. frequency (ν)	$0.3-50$ MHz	$0.3-10$ MHz	$0.5-60$ MHz	$0.3-30$ MHz
Instantaneous BW ($\Delta\nu$)	100kHz	1 MHz	1MHz	≥ 1 MHz
Obs. wavelength (λ)	$600-6$ m	10^3-30 m	$600-5$m	10^3-10m
Longest baseline	30 km	100 km	30 km	100 km
Spatial resolution	$0.6'$ at 50MHz	$1'$ at 10MHz	$0.5'$ at 60MHz	$0.3'$ at 30MHz
Array architecture	Centralized	Centralized	Centralized	Distributed
Estimated Mass	~ 200kg†, ~ 10kg‡	~ 550kg†, ~ 100kg‡	~ 500kg†, ~ 10kg‡	≤ 5kg
Deployment location(s)	Sun-Earth L2	Dynamic solar orbit, Moon far side, Sun-Earth L2	Sun-Earth L2	Earth/Moon orbit

Table 1: System requirements of recent space-based aperture array feasibility studies for ultra-long wavelength observations, namely FIRST (12), DARIS (63; 15), SURO-LC (7), and OLFAR (11; 59), where † and ‡ denote the daughter nodes and the mothership respectively.

1.3 Overview

The purpose of this article is to discuss the current technological advances towards the feasibility of space-based array for radio astronomy at ultra-long wavelengths. To this end, we elaborate on the system design for a space-based array in Section 2. We address various subsystems of the potential satellite array in the Sections 3 - 6, including the astronomy antenna design in Section 3. Although the current technologies limit the number of satellites to ≤ 10, we foresee next generation arrays to contain a larger number of satellites, which would behave as a co-operative wireless network. Hence, a dominant theme of the article is to investigate the extension of the proposed centralized solutions to distributed scenarios, particularly for processing (Section 4), communication (Section 5), and for joint position-time estimation of the satellites in the network (Section 6). We summarize the article with a brief overview of the potential deployment locations (Section 7), and the fundamental challenges ahead for a space-based ULW array (Section 8).

2 Ultra-long wavelength interferometry

2.1 Aperture synthesis

Radio astronomy imaging is achieved by aperture synthesis, wherein the cosmic signals received at a large number of time-varying antenna positions, are coherently combined to produce high quality sky maps. Each antenna pair forms a baseline of an interferometer, and a N element antenna array leads to $\bar{N} \triangleq 0.5N(N-1)$ unique sampling points at a given time instant. Let $\mathbf{x}_i(t)$ and $\mathbf{x}_j(t)$ be two arbitrary antenna position vectors which form a baseline at time t, then the corresponding uvw point is defined as

$$[u_{ij}(t), v_{ij}(t), w_{ij}(t)]^T \triangleq (\mathbf{x}_i(t) - \mathbf{x}_j(t))/\lambda, \tag{1}$$

where λ is the observed wavelength. Figure 1(a) shows the uvw points (in blue) for a $N = 9$ satellite cluster observing at 10MHz, and arbitrarily deployed with a maximum distance separation of d=50km. The effective synthesized aperture is then obtained by projecting the uvw points onto a 2-D plane which is orthogonal to the source direction. As an illustration, Figure 1(a) shows 3 such projections (in black) for sources orthogonal to the uv, uw and wv planes. The minimum distance between the satellites is typically only constrained by practical

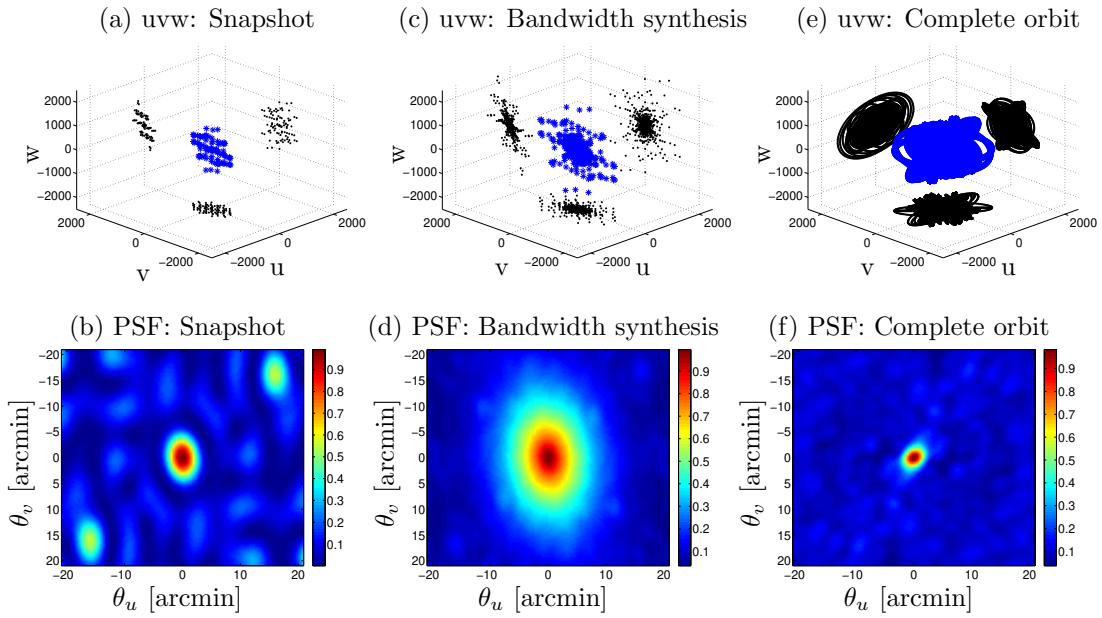

Figure 1: Aperture filling of a 9-satellite ULW array for an Heliocentric Earth-leading orbit around the Sun, to illustrate the effect of the sampling space on the normalized Point Spread Function (PSF). The figure in (a) shows the uvw coverage for the 3-D array of satellites at $\nu = 10$MHz for a single snapshot $N_t = 1$, and the corresponding PSF is displayed in (b). Bandwidth synthesis is illustrated in (c) which shows the uvw coverage of single snapshot imaging using 10 frequency bins, which are uniformly distributed in the range $1 - 10$MHz, and the resultant PSF is displayed in (d). The figures in (e) and (f) show the UVW coverage and corresponding PSF of the 9-satellite ULW array, for an entire orbit around the sun at 10MHz with a single observation each day, i.e., 365 snapshots.

safety requirements, and the maximum distance d between the satellites defines the resolution (θ) of the interferometric array i.e.,

$$\theta = \lambda/d. \tag{2}$$

The Van Cittert-Zernike theorem relates the spatial correlation of these antenna pairs directly to the source brightness distribution by a Fourier transform (71). Hence for radio imaging, each antenna pair output is cross-correlated to measure the coherence function, which is then subsequently converted to a sky map by an inverse Fourier transform. For a single point source along the w direction, the Figure 1(b) shows the normalized Point Spread Function (PSF) corresponding to the aperture coverage in Figure 1(a). A densely sampled aperture plane lowers the spatial side-lobes of the sky image, which are visible in Figure 1(b). The filling factor of the synthesized aperture can be increased by either by populating sufficient baselines or by using bandwidth synthesis. In bandwidth synthesis, different frequency channels can be used to scale λ. As illustrated in Figure 1(c) and Figure 1(d), with only 10 frequency bins uniformly distributed across $1 - 10$MHz, the aperture filling and the PSF is significantly improved as compared to Figure 1(b). Alternatively, the number of baselines can be increased by the increasing the number of satellites/antennas, or by populating uvw points over time-varying antenna positions. A first-order uvw simulation of an array comprising of $N = 9$ satellites in a Heliocentric Earth-leading orbit yields Figure 1(e) where one snapshot per day was assumed at an observation frequency of 10MHz, and the resulting PSF is shown in Figure 1(f). The number of uvw points are directly related to the unique number of baselines, and the observational bandwidth. To achieve the confusion limit and to resolve the sources individually, the total number of unique uvw points over the observational time period must be larger than the total number of detected sources.

2.2 Ultra-long wavelength sky

The dominant foreground in the low frequency radio sky is the galactic synchrotron radiation, which is due to synchrotron emission from the electrons moving in the galactic magnetic field. This emission causes the brightness temperature to rise from $\sim 10^4$K at 30MHz, to as high as $\sim 10^7$K around 2MHz (54). At frequencies below 2MHz, the Galactic plane is nearly completely opaque and the extra-galactic sources cannot be observed. More concretely, for frequencies above 2MHz, the sky temperature can be approximated as (34)

$$T_{sky} = 16.3 \times 10^6 \mathrm{K} \Big(\frac{\nu}{2\mathrm{MHz}}\Big)^{-2.53} \quad \text{at } \nu > 2\mathrm{MHz}, \tag{3}$$

where ν is the observation frequency. For Earth-based observations at higher frequencies ($>$ 100MHz), the overall system noise temperature T_{sys} plaguing the cosmic signal is typically dominated by the noise from receiver electronics T_{rec}. However, at lower frequencies, the intense galactic background implies that T_{sky} will be at least an order of magnitude larger than T_{rec}, and hence the overall noise temperature $T_{sky} \gg T_{sys}$. The immediate effect of this extremely high sky noise is the poor sensitivity of the interferometric array. The 1σ RMS sensitivity of an N element array (25), is given by

$$S_\sigma = \frac{235.6\ T_{sys}}{\lambda^2 \sqrt{N(N-1)(t_{obs}/1\mathrm{hour})(\Delta\nu/1\mathrm{MHz})}}\ \mathrm{mJy/beam}, \tag{4}$$

where $\Delta\nu$ is the bandwidth, t_{obs} is the observation time period over which the signal is integrated and the total number of estimated sources above this sensitivity is given by

$$N_>(S) = 1800\ \mathrm{deg}^{-2} \big(S/10\mathrm{mJy}\big)^{-1.3} \big(\nu/10\mathrm{MHz}\big)^{-0.7}. \tag{5}$$

Furthermore, the scattering in the interplanetary media (IPM) and interstellar media (ISM) also hinder observational frequencies less than 30MHz, which limit the maximum baseline between the satellites to

$$d_{ISM} = 47\mathrm{km} \times (\nu/1\mathrm{MHz})^{1.2} \qquad \text{and} \qquad d_{IPM} \approx 10\mathrm{km} \times (\nu/1\mathrm{MHz}). \tag{6}$$

For very long baseline interferometry, the angular broadening of radio sources due to interstellar scattering will cause interplanetary scattering to be greatly reduced (44). Finally, the lower limit of the achievable noise is not the RMS sensitivity of the array, but the confusion limit. The presence of unresolved sources with individual flux densities below the detection limit leads to a constant noise floor, that is reached after a certain observation time t_{obs} (34). For extra-galactic observations, under certain nominal assumptions, this anticipated confusion limit due to background sources is

$$S_{conf}(\theta, \nu) = 16\mathrm{mJy} \times (\theta/1')^{1.54} (\nu/74\mathrm{MHz})^{-0.7}, \tag{7}$$

where θ is the effective resolution for which the flux is below the confusion limit. The confusion limit is the lower limit to the achievable noise floor and thus is an upper limit to the useful collective area of the array. In other words, adding more antennas only decreases the time in which the confusion limit is reached, but not the overall array sensitivity (4). The time necessary for an array to reach this confusion limited sensitivity is given by the "survey equation"

$$t_{survey} = 3.3\ \mathrm{days}\ \big(N/100\big)^{-2} \big(10\nu/\Delta\nu\big) \big(\nu/1\mathrm{MHz}\big)^{-0.66} \big(\theta/1'\big)^{-3.08}, \tag{8}$$

for $\nu > 2$MHz (14). Using these elementary and yet fundamental equations, a preliminary design for a space-based array can be proposed for desired science cases. For a more detailed study, refer to (34).

Parameter	Notation	Units	Equation	Extra-galactic survey					
Sensitivity	S_σ	Jy	Input	6.5E-02	6.5E-02	6.5E-02	6.5E-02	6.5E-02	6.5E-02
Baseline	d	km	Input	100	100	100	100	100	100
Obs. Time	t_{obs}	hours	Input	24	720	8760	720	8760	8760
Obs. frequency	ν	MHz	Input	10	10	10	10	10	30
Bandwidth	$\Delta\nu$	MHz	Input	1	1	1	3	3	3
Resolution	θ	arcmin	(2)	1.03	1.03	1.03	1.03	1.03	0.34
System temperature†	T_{sys}	K	(3)	2.8E+05	2.8E+05	2.8E+05	2.8E+05	2.8E+05	1.7E+04
No. of Antennas	N		(4)	229	42	12	25	7	4
ISM Max. Baseline	d_{ISM}	km	(6)	7.4E+02	7.4E+05	7.4E+05	7.4E+05	7.4E+05	2.8E+06
IPM Max. Baseline	d_{IPM}	km	(6)	100.0	100.0	100.0	100.0	100.0	300.0
Confusion limit	S_{conf}	Jy	(7)	0.07	0.07	0.07	0.07	0.07	0.01
Resolution (Conf. lim.)		arcmin	(4), (7)	1.00	1.00	1.00	1.00	1.00	1.65
Max. Baseline (Conf. lim.)		km	(2), (7)	103.09	103.09	103.09	103.09	103.09	20.86
Time to Conf. lim.		hours	(8),(7)	0.14	4.05	46.39	3.98	43.64	38.94

Table 2: The system parameters needed to achieve a resolution of $1'$ and sensitivity of 65mJy, for various choices of observation time, observation frequency and instantaneous bandwidth. † indicates sky noise dominated.

2.3 System definition

The science cases for an ULW array broadly span cosmology, galactic surveys, transients from solar and planetary bursts and even the study of Ultra-High Energy particles. Although a single satellite mission would suffice to detect the global dark-ages signal, over 10^4 antennas are required to investigate the radio emission from Extrasolar planets (see 34, Table 1). For a first space-based ULW array however, with possibly only a few satellite nodes, extra-galactic surveys and study of transients are among the best suited science cases (14), which we present as case studies. The proposed space-based array design can be readily extended to cater to other science cases, e.g., detection of the global dark-ages signal.

The expected signal strength for the extra-galactic surveys is in the order of 65mJy with a desired spatial resolution of $\sim 1'$. In Table 2, we present different scenarios to investigate the effects of varying observational frequencies, bandwidth and observation time, on the number of antennas to achieve 65mJy. It is evident that increasing the observation time (1 day, 1 month, 1 year) steadily reduces the required number of antennas. Secondly, increasing the bandwidth from 1MHz to 3 MHz is also an alternative to achieve the desired resolution for a smaller array. However, the increase in bandwidth has little effect on the confusion limit. We note that the confusion limit is a bottleneck for shorter integration times and lower observing frequencies. The maximum baseline is in general confusion limited for frequencies $\geq$ 10MHz, however at $<$ 10MHz, the ISM and IPM scattering limits the maximum baseline and subsequently the resolution. At 10MHz, we require at least one year of observation time with more than 7 antennas for an observational bandwidth of 3MHz to achieve the 65mJy sensitivity. However, in the last column of the Table 2, we see that at 30MHz, only 4 antennas are sufficient. Such a configuration is estimated to detect over a million sources using (5). These small array of antennas are adequate if arbitrarily long observations are possible, which may be limited by rapid, strong radio bursts from the Sun and Jupiter, and possibly high relative satellite motion. In such scenarios, quasi-snapshot imaging may be necessary, and consequentially a larger number of antennas may be needed.

A similar investigation was conducted for Jupiter-like flares and Giant crab-like pulses, which are bright events with order of MJy and kJy respectively, with typical time scales of milliseconds. The desired resolution for these transient radio systems are $\sim 1'$ at frequencies below 30MHz. Since these events are extremely bright, even a single antenna with a nominal bandwidth of 10% of observational frequency would meet the desired requirements. However, unlike the extra-galactic surveys, the observations for these scenarios, are not confusion limited, but possibly by the number of baselines for short integration timescales of milliseconds. The number of unique

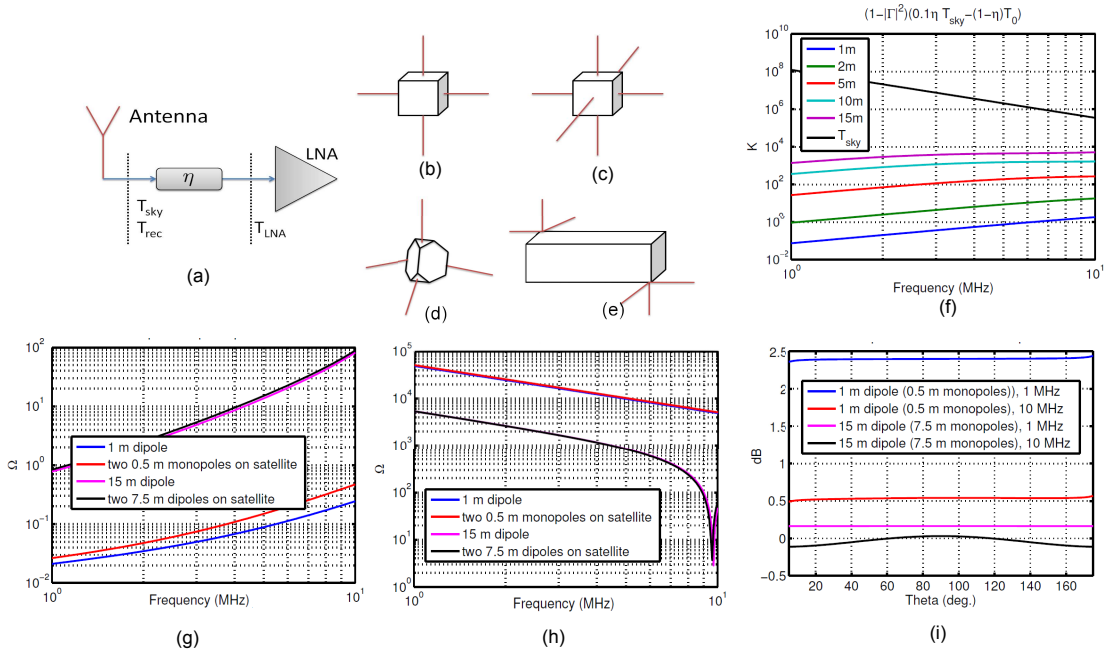

Figure 2: (a) A system model for an LNA connected to the space-based antenna (b) Configuration of a dipole antenna on a cubesat (c) Configuration of a tripole antenna in a cubesat (d) four monopoles (e) A dipole antenna placed on the opposite ends of a 3U-cubesat (f) Required T_{LNA} as a function of frequency for non-matched dipoles of varying lengths. (g) Real part of input impedance and (h) Absolute value of imaginary part of input impedance for two monopoles placed on a satellite compared to a dipole (i) Ratio of gain of two monopoles placed on a satellite and a dipole.

uvw points will depend on the deployment location and the relative velocities of the antennas. However, in general this limitation can be overcome by increasing the integration times in both these cases by over a minute.

In general, higher bandwidth, higher observing frequencies and longer integration times require less antennas to reach the same sensitivity level. In this article we choose the DARIS mission specifications as a reference to illustrate various sub-systems. To this end, we particularly focus on an array of N=9 satellites, with a maximum satellite separation of 100km and capable of observing the skies at $0.1-10$MHz. This particular setup meets the requirements for the extra-galactic survey and transient radio system science cases. In general, all the proposed techniques and technologies in the following sections can be readily extended to for larger arrays and larger observation spectrum.

3 Radio astronomy antenna design

We begin our discussion with the design of the observational antenna, which is a critical component for the space-based array. The system model of the observation antenna connected to a low noise amplifier (LNA) is shown in Figure 2(a), wherein the antenna is modeled as an ideal lossless antenna, followed by an attenuator, which is representative of the antenna losses. For the observation frequencies of $0.3-30$MHz, this front end must be sky noise limited i.e., $T_{rec} < 0.1T_{sky}$, where T_{rec} is the receiver noise and T_{sky} is the sky noise temperatures, which are defined at the interface between the lossless antenna and attenuator. The LNA noise temperature T_{LNA} defined at the input of the LNA is equal to $(1-\eta)T_0$, where η is the radiation efficiency and T_0 is the physical temperature of the antenna (chosen as 290K). Without loss of generality, we assume that the LNA noise is dominant over the noise contribution of subse-

quent electronics of the receiver. Under these assumptions, the prerequisite on the LNA noise temperature is derived as

$$T_{LNA} < (1 - |\Gamma|^2)(0.1\eta T_{sky} - (1 - \eta)T_0), \tag{9}$$

where Γ is the reflection coefficient of the antenna (6). A straightforward candidate for the observation antenna is a dipole (e.g., Figure 2(b)), which can be realized by rolling out metallic strips from the satellite (49). The observational wavelengths are much larger compared to the dimensions of the satellites and hence, due to practical limitations, the realized dipole will be short compared to the wavelength. For instance, the classic half-wave dipole for 10MHz and 30MHz observation frequencies yields a dipole length of 15m and 10m respectively. For lower frequencies, this dipole length begets a similar directional pattern, but with less directivity. Consequentially, the radiation resistance of the smaller antenna would be low, and the thermal noise will significantly dominate the total antenna noise.

To maximize the received power at the antenna, matched dipoles can be used, in which case $\Gamma \approx 0$. However, the combination of antenna and matching network becomes highly resonant with a high quality factor, and therefore significantly limiting the achievable bandwidth of the system, in particular for shorter dipoles. Hence, we propose the use of a non-matched dipole (6). Using (9), we have the Figure 2(f), which shows the T_{LNA} for varying lengths of non-matched dipole lengths. We use a LNA with input impedance of 2KΩ, which is a pragmmatic value for an LNA using a bipolar transistor. While the T_{LNA} is above 100K for 10m and 15m antennas, the required noise temperature for shorter dipole lengths are significantly lower, especially for lower frequencies.

In practice, a dipole is implemented on a satellite using two monopoles. To verify the validity of the proposed model, impedances of two monopoles on a satellite body is compared to that of the dipole. The satellite body under simulation is modeled as a cube of $40 \times 40 \times 40$cm, with perfect conducting surfaces. Furthermore, since the impedance of the monopole above a perfect ground plane is half the impedance of a dipole, the impedance of the monopole is multiplied by a factor 2 in the simulations for a fair comparison. Figure 2(g) and Figure 2(h) show the real component of the impedance and absolute value of the imaginary component of the impedance respectively, for 1m dipole versus 0.5m monopoles, and 15m dipole versus 7.5m monopoles respectively. As observed in these figures, there is negligible difference between the dipole and the two monopole configuration. A step further, we compare the ratio of gains between a pair of monopoles against the 1 meter and 15 meter dipoles at 1 and 10MHz. The investigated antenna lengths the ratio of gain are almost flat across for varying angles as observed in Figure 2(i), which indicates the element pattern does not change if a configuration of two monopoles is used instead of a dipole.

Two orthogonal dipoles (Figure 2(b)) are in theory sufficient to get all the polarization information of the cosmic signal, however a tripole (i.e., three dipoles, see Figure 2(c)) can be used to obtain information of all 3 components. The third dipole improves the directivity of the antenna system, thereby increasing the field of view. Along similar direction, an equiangular four monopole configuration can also be considered, as shown in Figure 2(d). However, the number of correlations is much higher, and consequentially demanding more signal processing hardware for each antenna. In the OLFAR study where a $3U$-cubesat ($30 \times 10 \times 10$ cm) is utilized, the monopoles are deployed in groups of three at the opposite ends of the satellite, as seen in Figure 2(e). The asymmetric design changes the properties of the monopoles and reduces the purity of the independent components, which was studies (65), and later experimentally evaluated on a smaller scale (56).

Data rates and processing	Notation/Equation	Value	Units/Remark
No. of satellites (or antennas)	N	9	(scalable)
No. of polarizations	N_{pol}	3	
No. of channels/signals	$N_{sig} = N_{pol}N$	27	
No. of bits	N_{bits}	1	bits
Observation frequency	ν	≤ 10	MHz
Instantaneous bandwidth	$\Delta\nu$	1	MHz
Spectral resolution	$\Delta\nu_{res}$	1	kHz
No. of bins	$N_{bins} = \Delta\nu/\Delta\nu_{res}$	1000	
Snapshot integration time	τ	1	second
Observed data rate	$D_{obs} = 2\Delta\nu N_{pol}N_{bits}$	6	Mbps/satellite
Centralized			
mothership data reception	$D^c_{in} = D_{obs}(N-1)$	48	Mbps
Earth down link data rate	$D^c_{out} = 2N^2_{sig}N_{bits}N_{bins}/\tau$	1.46	Mbps
Distributed			
No. of sub-bands	$N_{sb} = N$	9	
Sub-band bandwidth	$\Delta\nu_{sb} = \Delta\nu/N_{sb}$	111.11	kHz
Inter-satellite reception	$D^d_{in} = D^c_{in}/N$	5.34	Mbps/satellite
Earth down link data rate	$D^d_{out} = D^c_{out}/N$	162.2	kbps/satellite

Table 3: Data rate estimates for a *Centralized FX correlator* and a *Frequency-distributed FX correlator*, for the DARIS mission of 9 satellites.

4 Digital Signal Processing

Sky images in radio astronomy are made by calculating the Fourier transform of the measured coherence function (70). The coherence function is the cross correlation product between two antenna signals located at the two spatial positions, averaged over a period of the integration time τ, which is typically implemented using a correlator. However, prior to the correlator, the signals from the antenna are pre-processed and digitized.

A typical pre-processing unit at each satellite node is illustrated in Figure 3, where each satellite generates $D_{obs} = 2\Delta\nu N_{pol}N_{bits}$bps, where N_{bits} is the number of bits and N_{pol} is the number of polarizations. Observe that with $N_{pol} = 3$, for a signal with nominal instantaneous bandwidth of $\Delta\nu = 1$MHz, sampled with $N_{bit} = 1$bit resolution, the output data rate is an estimated 6Mbps. Given a far-away deployment location, such as Lunar orbit ($\sim 400,000$ km) or Earth leading/trailing ($\sim 2\times10^6$ to $\sim 4\times10^6$ km), this down-link data rate burdens on the limited resources of a small satellite using current technology. Hence, the satellite cluster must not only employ on-board pre-processing of astronomical signals, but also on-board correlation to minimize down-link data rate back to Earth. To this end, either a centralized or a distributed correlator can be employed as illustrated in Figure 4.

The digitzed pre-processed signals must be correlated, which is typically accomplished by either an XF or an FX architectures. In the traditional XF correlator the signals are *i.e.*, cross correlated first and then Fourier transformed later, while the more recent FX correlator directly measures the cross-power spectrum between the two antenna signals (20). Although the XF architecture is beneficial because bandwidth can be traded for spectral resolution, the FX architecture offers computational efficiency, which is explained as follows.

Consider a N element antenna array, with N_{pol} polarization each, then the total number of channels/signals from all the satellites/antennas is given by $N_{sig} = N_{pol}N$. The processing

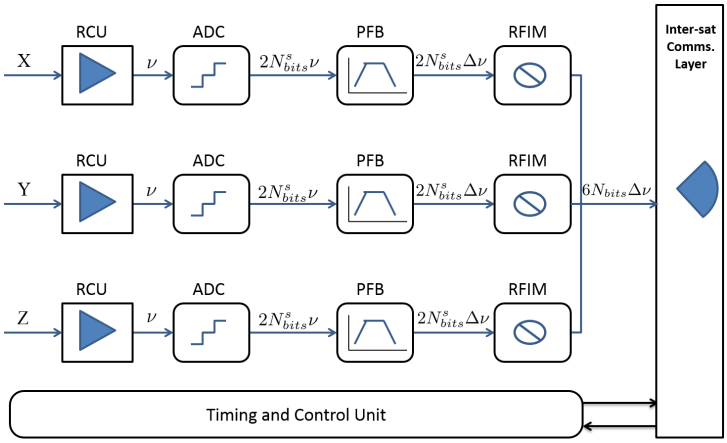

Figure 3: The $N_{pol} = 3$ polarized astronomical signals received by each antenna is signal conditioned and Nyquist sampled with a 14-bit (or more) analog to digital converter (ADC). A coarse Poly-phase filter bank (PFB) is used to selectively choose the desired instantaneous bandwidth of $\Delta\nu = 1$MHz. After successful RFI Mitigation (RFIM), only $N_{bits} = 1$-2bits will be used in further processing stages (4). The total data generated for N_{pol} signal paths in each satellite is $D_{obs} = 6\Delta\nu N_{bits}$bps, which is transported to the inter-satellite communication layer.

factor for XF vs FX is given by

$$N_X^{xf/fx} = \Big(\frac{N_{sig}N_{bins}}{N_{sig} + \log_2 N_{bins}}\Big), \tag{10}$$

where $N_{bins} = \Delta\nu/\Delta\nu_{res}$, $\Delta\nu$ is the instantaneous bandwidth and $\Delta\nu_{res}$ is the spectral resolution (58). Observe that the multiplicands in the XF mode, are additive in the FX mode, besides the $\log_2$ reduction on the number of frequency bins. Therefore, although for a lower number of satellites/antennas the XF is comparable to FX mode, for large scalable array the FX mode is computationally cost effective. Since we envision a scalable space-based array, the FX architecture is chosen as the preferred architecture . Table 3 shows data rates for a cluster of $N = 9$ satellites, with an instantaneous bandwidth of $\Delta\nu = 1$MHz, and $\tau = 1$ second integration time. We now briefly compare the centralized FX versus distributed FX architectures.

4.1 Centralized architecture

In the centralized FX correlator framework each satellite node transmits $D_{obs} = 2\Delta\nu N_{pol}N_{bits}$bps to the centralized mothership, which in turn receives a total data rate of $D^c_{in} = D_{obs}(N-1)$bps, excluding the data collected from the antenna on the mothership itself. The input data from all satellites is then correlated and the output is transmitted down to Earth at the rate of $D^c_{out} = (2N^2_{sig}N_{bins}/\tau)$bps, where $N_{bins} = \Delta\nu/\Delta\nu_{res}$. A significant drawback of the centralized correlation is that it depends heavily on the healthy operation of a single correlation station, which introduces a single point of failure (SPOF) for large array of satellites.

4.2 Distributed architecture

To alleviate SPOF, a frequency distributed correlator is proposed where each node is pre-assigned a specific sub-band $\Delta\nu_{sb}$ of the observed instantaneous bandwidth $\Delta\nu_{sb}$ for cross correlations (58). Hence, in addition to the node pre-processing (Figure 3), a secondary fine polyphase filter bank (PFB) is implemented to further split the instantaneous bandwidth $\Delta\nu$ into N_{sb} sub bands, each of bandwidth $\Delta\nu_{sb} = \Delta\nu/N_{sb}$. Each satellite is assigned a specific

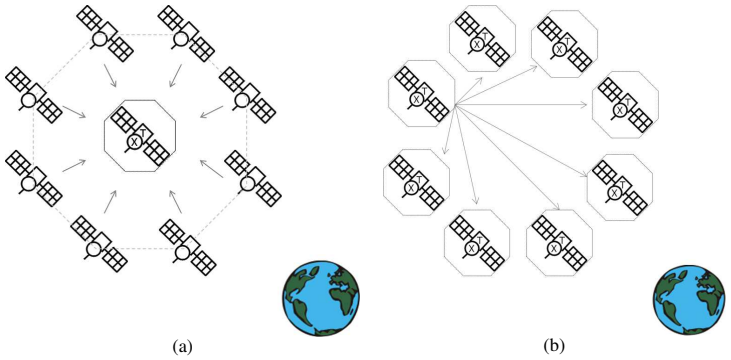

Figure 4: ***Correlator architectures:*** An illustration of two potential correlator architectures for space-based radio interferometric array, where the tags 'X' and 'T' on the nodes indicate correlation and transmission to Earth capabilities respectively. In the **(a) centralized correlator** architecture a centralized mother ship receives data from all observational satellites, correlates and down-links data to Earth. On the contrary, in the **(b) distributed correlator** framework, the observed data is evenly distributed between all nodes, and after post correlation all the satellite nodes down-link their respective correlated data to Earth.

sub-band for processing and the other $(N_{sb} - 1)$ sub-bands are transmitted to corresponding satellites via the intra-satellite communication layer. Furthermore, for even distribution of data and to ensure scalability, we enforce the number of sub-bands equal to the number of satellite nodes, *i.e.*, $N_{sb} = N$. Subsequently, in the distributed framework, each node receives a specific sub-band of the observed data, i.e., (D_{obs}/N_{sb}) from $N - 1$ other satellites in the network which yields a total input of $D^d_{in} = (D_{obs}/N_{sb})(N - 1) = (D^c_{in}/N)$bps, and down-links $D^d_{out} = (D^c_{out}/N)$bps respectively.

Thus, the frequency distributed correlator reduces the inter-satellite communication by a factor N. Furthermore, at the cost of equipping all observational satellite nodes with communication capability (both inter-satellite and down-link to Earth), SPOF is averted and scalability is ensured. In the context of the projects discussed earlier, DARIS, FIRST and SURO-LC implement a centralized architecture, whereas OLFAR proposed the distributed FX architecture. Given the system frequency is typically an order of magnitude or more than the processing instantaneous bandwidth, computing requirements are negligibly small, which has been duly noted in almost all recently completed studies.

4.3 Clocks

The choice of the on-board clock on each satellite has a significant impact on the signal processing system . The short-term clock stability i.e., $t \ll 1$ second is dominated by the clock jitter, which limits the effective number of bits (ENOB) for a given observational frequency ν. Although 1bit resolution suffices, the potential array will digitize the observed signal at a higher data rate ≥ 12 bits, to ensure functionality in (possible) high-RFI deployment locations. For instance, to facilitate a 14-bit Nyquist sampling at the observational frequency ν, the chosen clock must have a short-term stabiliy i.e., $\delta t_{jitter} < 1$ps, as seen in the Figure 5a. Secondly, to evaluate clock stability over longer time periods *i.e.*, $t \gg 1$ seconds, we use Allan variance, which is a measure of nominal fractional frequency drift (8). Following (73; 71), the stability requirement on the clock is defined such that the RMS phase error of the clock remains less than 1 radian

$$2\pi\nu\sigma_\zeta(\tau_c)\tau_c \lessapprox 1, \tag{11}$$

where ν is the observational frequency, τ_c is the coherence time, and $\sigma_\zeta(\tau_c)$ is the Allan deviation as a function of τ_c (57). The product $\sigma_\zeta(\tau_c)\tau_c$ can be visualized as the time drift due to non-

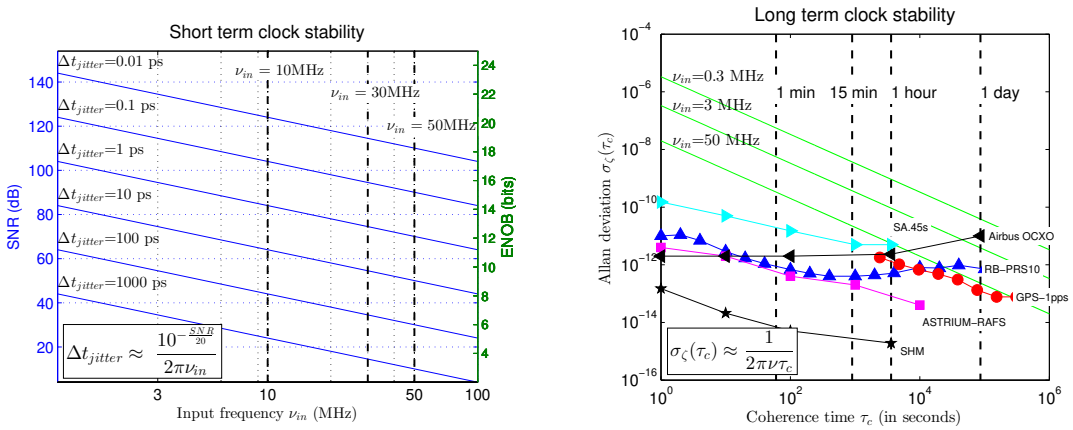

Figure 5: The short-term and long-term clock stability requirements for space-based radio astronomy. **(a)** Short term: The plot shows limiting cases of the Signal to Noise Ratio (SNR) and corresponding Effective Number of Bits (ENOB) due to jitter t_{jitter} versus input frequency ν . Three demarcation lines shows the maximum input frequency of $\nu = 10$MHz, $\nu = 30$MHz and $\nu = 50$MHz. **(b)** Long term: Desired Allan deviations of free running clocks are plotted versus the coherence time (in green) for various input frequencies ν_{in}. The map is overlayed with Allan deviations of potential clocks (in blue) for potential space-based low frequency arrays namely PRS-10 Rubidium (68) , ASTRIUM RAFS (26), GPS 1pps (46), Airbus OCXO-F (1), SA.45s (51) and space Hydrogen maser (SHM) (30).

linear components of the clock after τ_c seconds. Furthermore, the linear parameters of the clock i.e., frequency and phase offsets can be eliminated by exploiting the affine clock model, which is discussed in Section 6. Figure 5 shows expected Allan deviations of potential clocks versus the coherence time as per (11) for various input frequencies ν. Among the presented choices in Figure 5, the ASTRIUM RAFS (3.3kg, 30W) and Airbus OCXO-F (220g, 2W) are space qualified Rubidium and Oven controlled oscillators respectively. A particular clock of interest is the Chip-Scale Atomic Clock (CSAC) SA.45s, which is a Rubidium clock weighing less than 35 grams, consuming < 0.125W, and offers an coherence time of up to 15 minutes. Although the SA.45s is not space qualified, more recently, similar CSACs are available for space-based applications e.g., Airbus OCXO-H (2).

5 Communications

The potential communication scenarios for the envisioned space-based array are shown in Figure 6, which follow directly from the correlator architectures discussed in Section 4. A centralized architecture, as shown in Figure 6(a), comprises of a mothership collecting raw observed data from a cluster of daughter satellites and down-links the processed data to an Earth-based ground station. Alternatively, in case of the distributed scenario shown in Figure 6 (b), all satellites are capable of both exchanging data and correlating them, before down-linking back to Earth. In addition to the science data, housekeeping information is also exchanged between the satellites via tele-commands and telemetry, which is expected to be relatively small ($\approx$ 100kbps) in comparison to the astronomical data of 6Mbps. The housekeeping information is critical for control, timing and synchronization of the satellite, and to maintain coherence within the satellite network.

5.1 Inter-Satellite Link (ISL)

Implementing the inter-satellite link (ISL) using high-frequency optical communication has many advantages as compared to radio communication, such as reduced mass (and volume)

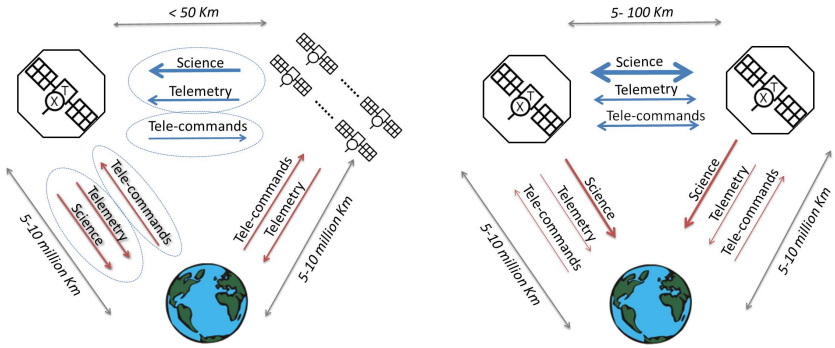

Figure 6: An illustration of a **(a)** centralized communication architecture and **(b)** single pairwise-link of a distributed communication architecture for a space-based radio interferometric array. The inter-satellite link is indicated in **blue** and the Earth-downlink by **red** . Telemetry and tele-commands are exchanged between the satellites and with Earth in both scenarios. In case of the centralized scenario, we assume the mothership is positioned at the center of the array with a maximum mothership-node distance of 50km.

of equipment, higher data rates, and no regulatory restrictions as experienced for radio frequency (RF) bands (67; 72) . However, this would also require extremely accurate alignment of the satellites, robust synchronization and more power than what could potentially be available for a small satellite. In the RF domain, orthogonal frequency-division multiplexing (OFDM) is an efficient modulation scheme for the ISL, in particular for a scalable antenna array with limited available bandwidth (53). OFDM is well suited to frequency selective channels and offers potentially a good spectral efficiency. The signals from each satellite node which form individual channels will be modulated using a form of phased shift keying (PSK), amplitude shift keying (ASK), or a combination quadrature amplitude modulation (QAM). In this article, we consider an ISL transmission frequency of 2.45GHz, although other frequency bands can also be used.

One of the potential solutions to implement the ISL is to use patch antennas on each face of a satellite node, such that the combined implementation yields a full coverage of the sky. All the satellites will have patch antennas on all six faces for both uplink and downlink. In addition, a diplexer will be used to separate the receiving and transmitting channels. Using a coaxial switch (controlled by the CPU) the desired signal is selected, amplified and finally detected at the satellite node. The communication antenna must have a bandwidth of 100MHz around 2.4GHz, with a reflection coefficient less than -10 dB between 2.35GHz and 2.45GHz, and the half-power beam-width must be at least 90°. Figure 7(a) shows the simulated patch antenna, where all dimensions are in millimeters. The patch is fed by a coaxial probe located 7.5mm from the center of the patch. It was observed that in case of a linearly polarised patch antenna, the given setup yields a -3 dB beamwidth less than 90° for the radiation pattern in the $\phi = 90°$ plane, which is less than our desired requirement. Thus, to improve the radiation pattern we implemented a circularly polarized patch antenna. Moreover, an added advantage is that the polarization of both transmit and receive antenna is independent of the orientation of the antennas with respect to each other. The circular polarization is realized by adding a second co-axial probe to the patch, shown in red in Figure 7(a). As seen in the Figure 7(b), the reflection coefficient is better than -10 dB in the frequency range $2.35 - 2.8$ GHz. Additionally, the radiation patterns in Figure 7(c) show the half-power beam width is more than 3dB, for both the $\phi = 0°$ and $\phi = 90°$ planes.

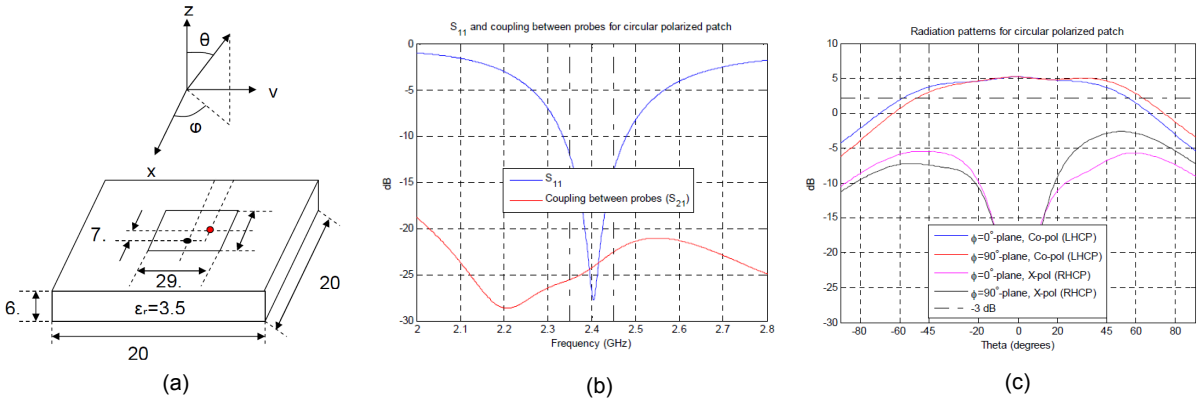

Figure 7: (a) The simulated patch antenna with dimensions in millimeters. (b) Reflection coefficient, and (c) Radiation patterns across desired frequency range.

5.2 ISL Link margin

Table 4 shows the ISL budget for the centralized and distributed scenarios. In case of the centralized scenario, we assume that the mothership is in the center of the array with a maximum mothership-node distance of 50km. To estimate the link margin for a centralized scenario, we assume that the mothership can transmit with a power of 1W i.e., 30dBm. Now, using the patch antenna gain of 3dBi and nominal losses (at the diplexer, transmitting cable and coaxial switch loss) of 2.6 dB, the equivalent isotropically radiated power (EIRP) of each satellite is 30.4dBm. For both the centralized and the distributed scenarios, the ISL channel in space is in principle free space loss, where multi-path, atmospheric losses, absorption losses and even Doppler effects can be ignored. Hence, the Friis free space loss for 2.4GHz transmission frequency and 50km is 134.7dB. Hence, the effective received power for an EIRP of 30.4dB and a pointing loss of 0.5dB is -104.80dB. The received C/N0 is estimated at 67.66dB/Hz, for a G/T ratio of -26.14 dB/K (see Table 4). The transmission data rate mothership to node is 100kbps (50 dB/Hz), which yields an Eb/No of 17.66dB. For a typical receiver, an Eb/No of 2.5dB is needed. Now, including a implementation loss of 2dB, the link margin for uplink with transmit power of 1W is 13.16dB. The downlink from the node satellite to the mothership, includes the 6Mbps science data (see Table 3) and the housekeeping data of 100kbps, which amounts to 6.10Mbps. This total downlink data rate can be established with a link margin of 2.29, and a transmission power of 5W.

Extending the link margin estimates of the centralized ISL architecture to a distributed scenario has two fundamental challenges. Firstly, the transmission data rate is now 5.44Mbps, which includes 5.34Mbps of science data (see Table 3) and 100kbps of housekeeping data. Secondly, in the absence of a centralized correlator, the maximum distance between the satellites is 100km, a factor 2 compared to the centralized scenario. Hence, to achieve the same link margin of 2.29dB as the node to mothership downlink, the transmission power of each satellite in the distributed architecture must be 4 times that of the centralized scenario, i.e., 20W. Although 15W suffices to achieve a positive link margin for the distributed architecture. This requirement is a bottle neck for scalable array of small satellites with limited transmission power. One possibility is to use clustering schemes and multi-hop approaches to reduces the communication distances between the satellites (19), which is a research area currently being explored (52).

	Parameters	Centralized $MS \rightarrow node$	Centralized $Node \rightarrow MS$	Distributed $Node \leftrightarrow Node$	Units
System Definition	Frequency band	2.45	2.45	2.45	GHz
	Maximum distance	50.00	50.00	100.00	km
	TX power	1.00	5.00	15.00	W
	Required datarate	0.10	6.10	5.44	Mbps
	Antenna gain	3.00	3.00	3.00	dBi
	Wavelength	0.12	0.12	0.12	m
ISL Channel	Free space Path losses	134.20	134.20	140.23	dB
	Atmospheric losses	0.00	0.00	0.00	dB
	Polarization losses	0.50	0.50	0.50	dB
	Absorption losses	0.00	0.00	0.00	dB
	Path loss	134.70	134.70	140.73	dB
Link Budget	TX power	30.00	36.99	41.76	dBm
	Loss coaxial switch	0.30	0.30	0.30	dB
	Diplexer losses	1.00	1.00	1.00	dB
	Cable losses	1.30	1.30	1.30	dB
	Transmit antenna gain	3.00	3.00	3.00	dBi
	EIRP of the spacecraft	30.40	37.39	42.16	dBm
	Pointing loss	0.5	0.5	0.5	dB
	Received power	-104.80	-97.81	-99.06	dBm
	Receiver G/T	-26.14	-26.14	-26.14	dB/K
	Bolzmann constant	-198.60	-198.60	-198.60	dBm/Hz/K
	Received C/N0	67.66	74.65	73.40	dB/Hz
	Data rate	50.00	67.85	67.36	dB/Hz
	Received Eb/No	17.66	6.79	6.04	dB
	Required Eb/No	2.5	2.5	2.5	dB
	Implementation loss	2	2	2	dB
	Link Margin	13.16	2.29	1.54	dB

G/T estimates	Gain (dB)	Temp (K)	Temp (dBK)	Loss (dB)	Tref (dBK)	Gref (dB)	Tref (K)
Antenna	3.00	100.00	20.00	-2.40	17.60	3.00	57.54
Coaxial Cable	-1.30	75.02	18.75	-1.10	17.65	-1.30	58.23
Diplexer	-1.00	59.64	17.76	-0.10	17.66	-1.00	58.29
Coaxial Cable	-0.10	6.60	8.20	0.00	8.20	-0.10	6.60
LNA	30.00	288.63	24.60	0.00	24.60		288.63
Backend	30.00	2610.00	34.17	-30.00	4.17		2.61
LNA Noise Figure (dB)	3.00				**G (dB)**	**0.60**	
Backend Noise Figure (dB)	10.00			**Totals**	**T (K)**		**471.90**
Ambient Temperature (K)	290.00				**G/T (dB/K)**		**-26.13**

Table 4: ***Inter-sallite communication:*** (Above) The Inter-Satellite Link (ISL) budget for centralized and distributed scenarios for a satellite array. (Below) Antenna gain to noise tempearature (G/T) estimates.

5.3 Space to Earth Downlink

The total downlink data rate D^c_{out} after correlation quadratically increases with the number of nodes in the cluster, and linearly reduces with the integration time (see Table 3). For a cluster of 9 satellites, with 1 second integration interval this rate is $\geq$ 1.46Mbps. In the DARIS study, the space to earth downlink was achieved using an X-band downlink unit (XDU). Figure 8 shows the X-Band transmit chain which consists of a modulator and a 60W traveling wave tube amplifiers (TWTA). In the nominal operation case the data is directly BPSK modulated on the X-band carrier at 4.3Mbps, amplified, filtered at the diplexer and transmitted via the high gain antenna (40dBi). During launch and early orbit phase and in contingency cases the transmission rate is reduced to 100bps, BPSK-modulated onto a subcarrier with low frequency (e.g., 8kHz) which itself PM-modulates the carrier. In order to enable full coverage two adversely polarized low gain antennas are transmitting into the two hemispheres. The receiver downconverts and demodulates the X-band data and feeds them to the OBC via RS422 link. In the nominal mode the command rate is 400kbps, BPSK-modulated on a 16kHz sub-carrier, and PM modulated onto the carrier. The estimated power consumption of the transceiver is 110W operational and 30W in standby. The high gain antenna (HGA), covering both the uplink and the downlink band, could be realized as a parabolic antenna similar to the one of Mars Express. With a

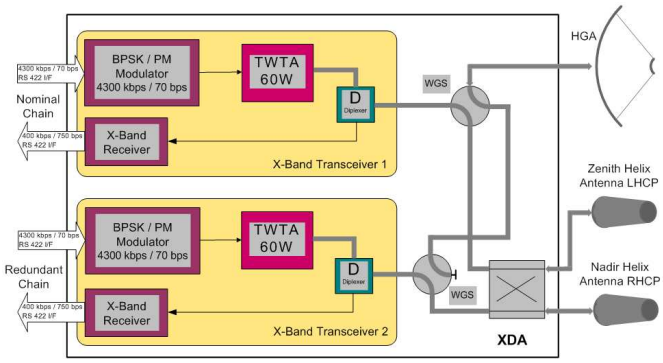

Figure 8: The XDU downlink solution proposed in the DARIS project. The XDU unit consists of a complete redundant transmit and receive subsystem, the X-band antennas and the interconnecting waveguide links. The X-Band downlink transceivers are directly interfaced to the Onboard Computer (OBC) via RS422. Two different modes are available for the communication link (a)Nominal link via High Gain Antenna (HGA) for science telemetry and commanding (b) Emergency link via low gain antennas (LGA) with full coverage and reduced data rates for telemetry and command.

40dBi design, the 3dB beamwidth would be around 1.7°, posing no significant challenge to the pointing mechanism. The low gain antenna (LGA) is a conventional helix antenna design covering also both transmit and receive band.

The number of ground stations on Earth are limited, and are therefore almost always in high demand. However, a 35m ground station with access for 8 hours per day suffices to meet the downlink data rate of upto 4.5Mbps for 9 nodes in Earth leading/trailing or Lunar Orbit. This requires a 1.5 m diameter parabolic antenna on board, with a one axis pointing mechanism to ensure the antenna can always point at the Earth as the satellite remains Sun pointed (14). For arrays larger than 50 satellites with energy constraints, it is difficult to establish Earth-based downlink with current off the shelf technology. However, these challenges and possible distributed downlink scenarios are currently being investigated (18).

6 Synchronization, Localization and Attitude determination

To maintain coherence between satellites, all the satellites must be synchronized, and their positions known up to sub-meter accuracies. These requirements on position-time accuracies at ULWs are considerably lower in comparison to other space-based array missions, such as LISA (13). Almost all Earth-based antenna arrays synchronize using GPS-aided atomic clocks, and their fixed antenna positions are known up to millimeter accuracy e.g., LOFAR (74). However, the envisioned space-based array will be deployed far-away from Earth-based GPS satellites, and unlike Earth-based antennas, these satellites will be mobile. In addition, given the large number of satellites and limited ground-segment capability, tracking each satellite independently is not pragmatic. Moreover, in certain deployment locations such as the Lunar orbit, the satellite array will be partially or even completely disconnected from Earth-based ground stations during eclipse periods.

Hence, the satellite array must be an anchorless network (i.e., without references), cooperatively synchronizing the clocks and estimating time-varying relative positions, in the absence of absolute reference on time and position. The estimated relative positions, which are identical to the absolute positions upto a rotation, are sufficient for inter-satellite communication, collision avoidance, and on-board correlation. For radio astronomy imaging however, to ensure the desired orientation of the projected baselines (see Figure 1), an external reference may be required occasionally to map the relative spacecraft positions on an inertial reference frame. Such an

absolute reference can be obtained by tracking a few satellites, during intermittent Earth-based communication.

In this section, we briefly discuss a dynamic ranging based solution to estimate the clock parameters and the time-varying distances of the network. Given these time-varying distance estimates, the relative positions over time can be estimated from distances, via MDS-like algorithms (16; 60). We are primarily interested in solutions for cold start scenarios, when no prior information is known. For longer time scales, when the orbital dynamics of the deployment location is well known, the estimated position-time parameters can be tracked and improved using recursive filters, e.g., Kalman Filter (40). In the end, attitude control for a satellite array is briefly addressed.

6.1 Joint ranging and synchronization

All clocks are inherently non-linear w.r.t. the ideal time t. However, a given clock can be approximated to a linear model, provided the Allan-deviation of the clock is relatively low for a small coherence time (see Section 4.3). More generally, let $\{t_i, t_j\}$ denote the local times at $\{i, j\}$ respectively, then the ideal time t is

$$t \triangleq \mathcal{C}(t_i,\ \dot{\psi}_i,\ \psi_i) \triangleq \mathcal{C}(t_j,\ \dot{\psi}_j,\ \psi_j), \tag{12}$$

where $\{\psi_i, \psi_j\}$ and $\{\dot{\psi}_i, \dot{\psi}_j\}$ are the phase and frequency offsets of a satellite pair $\{i, j\}$ and, $\mathcal{C}(\cdot)$ represents a linear function of the local clock parameters. However, in case of a satellite network, the pairwise distances are time-varying, which can be expanded as

$$d_{ij}(t) = r_{ij} + \dot{r}_{ij}t + \ddot{r}_{ij}t^2 + \ldots, \tag{13}$$

where $d_{ij}(t)$ is the time-varying distance between the satellite pair $\{i, j\}$ and $\{r_{ij}, \dot{r}_{ij}, \ddot{r}_{ij}, \ldots\}$ are range parameters of the Taylor expansion at ideal time $t = 0$ (61). More specifically, r_{ij} is the initial pairwise distance, $\dot{r}_{ij}$ is the range rate and $\ddot{r}_{ij}$ denotes the rate of range rate between the satellites. Given these pairwise distances, the relative positions of the satellites can be estimated using MDS-like algorithms (16). Our aim is to jointly estimate the clock parameters and the time-varying pairwise distances between the satellite nodes. The joint synchronization and ranging problem can be illustrated as shown in Figure 9, which shows a pair of asynchronous mobile satellite nodes. The mobile satellites transmit messages asymmetrically between each other, during which K time-markers are recorded at each end. Let $T_{ij,k}$ and $T_{ji,k}$ be the kth time-markers recorded at the ith and jth satellite nodes respectively, and $E_{ij,k} \in \{+1, -1\}$ indicate the transmit and receive direction of the message, then for any kth time instant, the generalized two-way ranging (GTWR) equation (61) is

$$\mathcal{C}_i(T_{ij,k}, \dot{\psi}_i, \psi_i) - \mathcal{C}_j(T_{ji,k}, \dot{\psi}_j, \psi_j) + E_{ij,k}d_{ij}\Big(\mathcal{C}_i(T_{ij,k}, \dot{\psi}_i, \psi_i)\Big) = 0 \quad \forall\{i, j\} \leq N\ , \forall k \leq K, \tag{14}$$

where without loss of generality the ideal time t of the time-varying distance $d_{ij}(t)$ is replaced with the clock model at satellite i (12). The unknown frequency offsets, phase offsets and the pairwise distances over K time instances can be estimated using the iterative mobile pairwise Least squares (iMPLS) and iterative mobile global Least squares (iMGLS). The iMPLS algorithm is applicable when the daughter satellite nodes communicate only with a centralized Mother-ship (i.e., Star network topology, see Figure 4a), whereby only the clocks of the satellites can be corrected. For a full mesh network, when all satellites communicate with each other (i.e., full mesh topology, see Figure 4b) both the clock parameters and the distances can be estimated, which is achieved by the iMGLS algorithm.

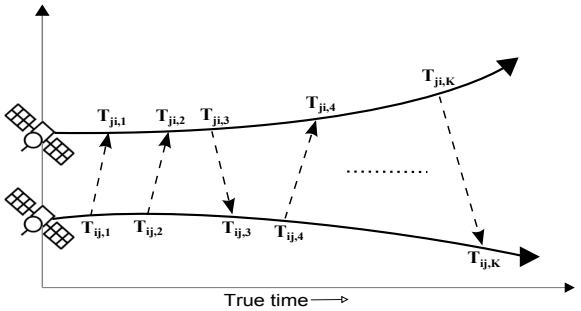

Figure 9: A generalized Two Way Ranging (TWR) scenario between a pair of *asynchronous mobile satellite nodes* where the asynchronous nodes transmit and receive asymmetrically, during which K time stamps are recorded at respective nodes. Unlike classical TWR (33) where the transmission and reception is alternating, the proposed setup imposes no pre-requisites on the sequence or number of two way communications. Consequently, this framework and proposed solutions for joint ranging and synchronization (61) can be readily extended to a plethora of TWR ranging protocols, including broadcasting and passive listening (64).

6.2 Simulations

To evaluate the performance of the algorithms, we consider a cluster of $N = 9$ mobile nodes in a $3-$dimensional Euclidean space. The initial frequency offsets $\dot{\boldsymbol{\psi}} = [\dot{\psi}_1, \dot{\psi}_2, \ldots, \dot{\psi}_9]$ and phase offsets $\boldsymbol{\psi} = [\psi_1, \psi_2, \ldots, \psi_9]$ of the nodes are arbitrarily chosen in the range $[-10^{-4}, 10^{-4}]$ and $[-1, 1]$ seconds respectively, where without loss of generality satellite node 1 is chosen as the reference node with $[\dot{\psi}_1, \psi_1] = [0, 0]$. Secondly, the initial positions $\mathbf{X}$ and initial velocities $\mathbf{Y}$, whose values are arbitrary chosen as

$$\begin{aligned}
\mathbf{X} &= \begin{bmatrix} 6.1 & -7.6 & -0.2 & 8.2 & 9.0 & -8.9 & 9.9 & 6.0 & -9.3 \\ -1.3 & 4.4 & 2.9 & -9.7 & -1.8 & -7.7 & -7.6 & 7.8 & 7.8 \\ 3.5 & 6.8 & 9.1 & 5.3 & 5.4 & 6.6 & 6.0 & 4.6 & 7.5 \end{bmatrix} \text{km}, \\
\mathbf{Y} &= \begin{bmatrix} -70 & -50 & -30 & -70 & -70 & 40 & -40 & 60 & 70 \\ 90 & 40 & 40 & -90 & -100 & 10 & -80 & -40 & 70 \\ 60 & 50 & 20 & 50 & 80 & 60 & 100 & 90 & 10 \end{bmatrix} \text{ms}^{-1}, \qquad (15)
\end{aligned}$$

For these assumed positions, the initial pairwise distance $\mathbf{r}$ is in the range $[0, 10]$ km. Secondly, for these values the range rates $\dot{\mathbf{r}}$ are arbitrarily distributed in the period $[-100, 100]$ m/s and the rate of range rate $\ddot{\mathbf{r}}$ are arbitrarily distributed over $[-10, 10]\text{m}^2/\text{s}$. These values are typically for worst case scenarios, assumed to evaluate the performance of the proposed algorithms. The mobile satellites communicate K messages with each other within a time interval of $[-1.5, 1.5]$ seconds, and the time-markers $T_{ij,k} \forall\ i, j \leq N, \forall\ K$ are generated accordingly. We assume alternating communication between the nodes and a Gaussian noise of $\sigma = 10^{-8}$ seconds($\sim$ 3.3 meters) plaguing the time-markers. Figure 10 shows the performance of the proposed algorithms for phase offset, frequency offset and pairwise distance estimation. The root mean square errors (RMSE) are plotted (in blue) against varying pairwise communications, from $K = 10$ to $K = 100$, where the clock parameters are averaged over N nodes and, the distances and range parameters are averaged over $\binom{N}{2}$ unique links. In addition, the theoretical lower bounds i.e., Cramér Rao Lower Bounds for the corresponding problem, are also plotted (in red), which is achieved asymptotically by the proposed estimators. To show the performance of the prevalent solutions, we also plot the low complexity Least squares (LCLS) which synchronizes the clocks for immobile network of satellite nodes. The iMGLS algorithm outperforms the iMPLS estimator since it exploits the full mesh communication network between the nodes. More significantly, the iMGLS estimator achieves clock accuracy of upto nanoseconds and distance errors up to meter accuracy at cold start.

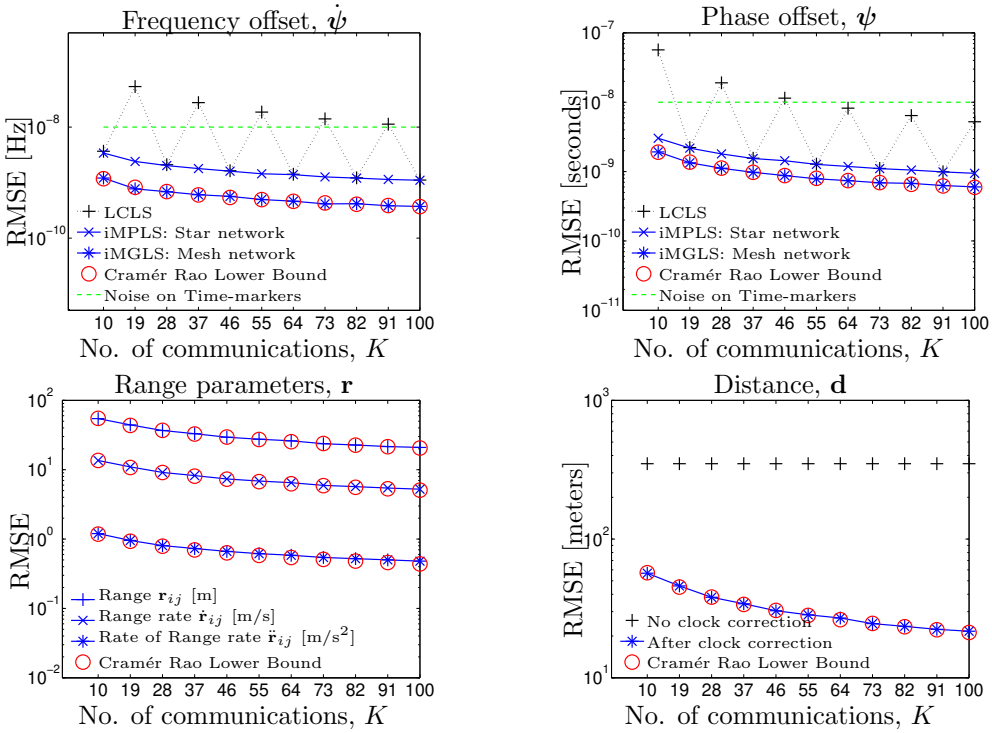

Figure 10: A simulation showing the root mean square errors (RMSEs) of the estimated frequency offset ($\hat{\dot{\phi}}$), phase offset ($\hat{\phi}$), range parameters ($\hat{\mathbf{r}}, \hat{\dot{\mathbf{r}}}, \hat{\ddot{\mathbf{r}}}$) and distance $\hat{\mathbf{d}}$ using the MGLS algorithm for joint ranging and synchronization.

An added advantage of using dynamic ranging is that the timestamps can potentially piggyback on the housekeeping data exchanged between the satellite nodes, which mitigates the need for a dedicated ranging system. However, if a ranging system is employed, then the achievable lower bound on the standard deviation for time Of arrival in multipath-free channels is given by

$$\sigma \geq \left(8\pi^2 F_c^2 BT \text{ SNR}\right)^{-1/2}, \tag{16}$$

where F_c denotes the carrier frequency, $B \ll F_c$ is the bandwidth of the signal, T is the signal duration in seconds (55) . The assumed noise variance on the time-markers in the simulation is $\sigma = 10^{-8}$ (shown in green in Figure 10), which can be adequately achieved by a satellite communicating at $F_c = 2.4$GHz with a nominal bandwidth of 1kHz, and SNR=10dB for a signal duration of $T \sim 1$ms.

6.3 Attitude determination

For estimating spacecraft orientation, two-vector attitude determination can be employed by the spacecrafts, where these vectors are either (a) the unit-vectors to the Sun and the Earths' magnetic field vector, or (b) unit vectors to two stars. The pointing direction for the satellites can be provided by commercially available sun and star trackers, which form an integral part of the Attitude and Orbit Control System (AOCS) in the satellites. Using these measurements, methods such as TRIAD or a solution to Wahbas' problem yield the on-board attitude determination (see 50, chap. 5).

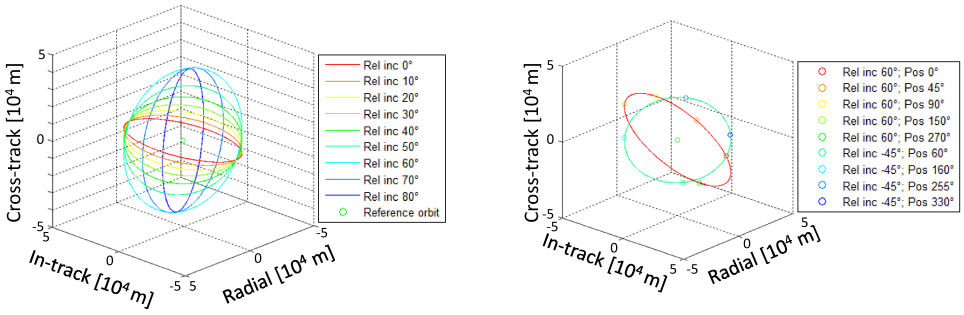

Figure 11: (Left) Relative orbits with different relative inclinations. (Right) Two relative orbits with several spacecraft in each orbit. These figures represent the relative orbits with respect to a reference orbit, with the Moon as the central body, and without any perturbations.

7 Deployment Locations

The deployment location of the space-based array must be chosen to ensure the following conditions be met.

- Low RFI during scientific observation cycles.
- Offer maximum possible down-link data rate.
- Provide sufficient positional stability during integration time τ.
- Remain within a sphere of $\sim$ 100km.

In addition, each satellite must offer low noise conditions with minimal EMC, stable temperature conditions, and stable gain. To alleviate the high complexity of active control to keep all the satellites within a cluster, passive formation flying could be employed. In passive formation flying paradigm, the satellites are allowed to drift, during which the relative positions and orientations of the satellites are constantly monitored. This approach eliminates the need for excess propulsion and heavy orbital maintenance equipment on all satellites. Additionally, the naturally varying position vectors of the satellites produce unique uvw sampling points, which consequentially improve the PSF (see Section 2.1

In order to avoid interference, either the cluster must be located far from Earth-based RFI and ionospheric distortions, such as Earth leading/trailing orbits and Sun-Earth Lagrangian points. However, by increasing the distance to the Earth, the communication with the Earth becomes more challenging. Alternatively, RFI shielding can be achieved by positioning the array on the far side of the moon. The radio astronomy explorer RAE-2 showed that the interference at very low frequencies is reduced by 2 orders of magnitude behind the moon, making it an ideal location for radio astronomy observations (3). However, during the eclipse behind the moon, the satellite cluster has no communication with Earth. The following section discusses the quest to find an optimum balance between down-link data rates and maximizing observation time, by emphasizing the challenges in various deployment locations.

7.1 Lagrange points and Moon-farside

The relative velocities of the satellites are minimal at the Lagrange points, and hence these locations offer increased positional stability for longer time intervals. Therefore, the Lagrange points are an optimal choice to increase the integration time of the observations, and also

ensure longer mission lifetime. The Earth-Moon L4 and L5 are much closer for Earth based communication, however are suspected to be less radio quiet relative to the Earth-Moon L2. The Earth-Moon L2 located at $\sim$ 61347km away from the Moon, is still in the cone of radio-silence, and is sufficiently shielded from RFI from Earth. However, this Lagrange point may not be a favorable deployment location, since transmission in this radio quiet zone may affect future missions (48). The Sun-Earth L4 and L5 points are too far and subsequently limit downlink rates. In contrast, the Sun-Earth L2 liberation point at $\sim$ 1.5 Million km away from Earth, is a trade off between downlink data rate, RFI avoidance and increasing coherence time. Although this is a stationary point, in practice a satellite operating at L2 will experience a gravity gradient with a slow and steady outward drift. Such a scenario is preferred by the FIRST (12) and SURO-LC (7) studies. The SURO-LC proposes a array of 8 daughter satellites drifting slowly in Lissajous orbit and a mothership at a fixed distance of 10km from the cluster. While such a mission will provide enhanced imaging performance with improved uvw coverage and longer integration times, the downlink data rate is estimated to be $2-3$ orders of magnitude less than a Moon based array using prevalent technology (59).

7.2 Orbiting the Moon

An equatorial orbit around the Moon presents a relatively easier down-link to Earth and sufficiently long eclipse times behind the Moon w.r.t. Earth. The long eclipse time periods shield against radio noise from Earth and enable the science observations. In the DARIS study, to increase the predictability of the relative positioning, the reference orbit around the Moon was chosen to be circular which additionally also decreases the chance of collisions (63). The array formation is build up from different relative orbits with a different relative inclination around a reference orbit (Figure 11(a)), where each of these relative orbits contain several node spacecrafts (Figure 11(b)). The reference orbit determines the duration of the eclipse time and subsequently the science duty cycle, which is increased by aligning an orbit with the Earth-Moon plane and/or by lowering the altitude (14). As seen in Figure 12, the Eclipse time period can be increased by decreasing the orbital altitude, however consequently the percentage of the orbit in the shade increases and thereby reducing the science duty-cycle. In addition, by decreasing the orbital altitude, the relative range rates of the satellites also increase, which in turn affects the baseline stability. Hence, a balance between the relative velocity and the eclipse time must be found. When including the perturbations of the Earths' gravity field, the irregularities in the lunar gravity field, the solar gravity field and the solar pressure, a constant drift of the relative orbits occurs. Coincidentally, this drift is typically dominant along the in-track direction of the reference orbit which can be compensated by adjusting the semi-major axis of the spacecraft. In essence, a circular orbit in the Lunar equatorial plane offers a stable orbit, provided a trade-off is achieved between eclipse time and the satellite range rates.

7.3 Heliocentric orbit

A potential reference orbit for formation flying around the Sun is the Earth orbit itself. However, if the satellites are too close to Earth, then the terrestrial interference is a major disturbance to science observations. Alternatively, an orbit around the Sun with a different eccentricity than the Earth orbit keeps the satellite array at 4 to 10 million km from Earth, which is far enough to offer both stability and also to reduce the radio noise from Earth. The large distance separation severely limits the available down-link bandwidth by at least an order magnitude compared to the Lunar orbits. In view of an optimal balance between increased data-downlink and RFI free science observation, we choose the Earth orbit as a reference orbit with the satellite nodes orbiting at a distance of 4 to 10 million km from Earth. Hence, even though the constellation

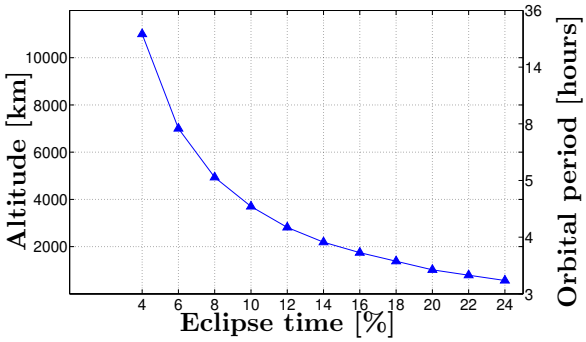

Figure 12: The plot shows the altitude vs Orbital period for a satellite in Lunar orbit. A satellite cluster orbiting the moon over the far-side enters a "cone of silence" behind the moon, once every orbit. During this phase, the moon shields the satellite cluster from Earth-based and solar interference and subsequently permitting relatively noise-free scientific observations. These eclipse periods can be extended by inserting the satellite network at a higher altitude, which also offers more orbital stability (59). However, a longer eclipse period behind the moon severly limits the communications with Earth.

orbits the Sun as a central body, the reference orbit does go around the Earth, from leading to trailing. One of the many benefits of this particular orbit is that it is relatively stable for 10 years and allows continuous scientific observations. However unlike the lunar orbital design, this reference orbit is eccentric and highly sensitive to small changes due to large difference between the semi-major axis and the relative pairwise distances of the satellites (14) (63). Furthermore, the time period of the reference orbit is equal to the period of the relative orbits, which causes the formation to drift in all directions. With reference to the reference orbit, the cluster will slowly expand with time and hence offers unique sampling points for interferometry. One of the key advantages of this orbit is the low relative range rates which facilitates longer integration period. For example, the relative range rates of the satellites in this orbit is estimated to be less than 20cm/s for 3 years (14). Despite this advantage, the solar orbit is sensitive to small errors in velocity and the relative orbits are stable only for change in injection velocities upto 0.1mm/s, which can be compensated using minor corrections (63).

8 Summary and Discussion

A satellite cluster of less than 10 nodes is scientifically very interesting and meets the requirements for the extra-galactic survey science cases in terms of resolution and sensitivity. At least 4 antennas observing at 30 MHz for more than a year is sufficient to achieve the confusion limit of 65 mJy with $1'$ resolution, in which case over a million sources can be detected (Section 2.3). Moreover, even with fewer antennas, transient science cases such as bright Jupiter-like flares and Crab-like pulses can be addressed. All the satellites will be equipped with 2 (or 3) 5m dipole antennas (or two 2.5 monopoles) to observe the $\leq$ 30MHz spectrum (Section 3).

For a nominal observational bandwidth of $\geq$ 1MHz, each satellite is estimated to generate $\geq$ 6 Mbits/s, which must be correlated in space to minimize downlink data rate to Earth. In both centralized and distributed scenarios, the processing requirements for filtering and correlation are negligibly small for up to 50 satellites and can be readily incorporated into the on board computer (OBC) (Section 4). To establish the inter-satellite link, the satellites will be equipped with patch antennas to transmit the desired $\geq$ 6Mbps data rate. The ISL budget analysis shows that in the centralized scenario, using 2.45GHz ISM band, the node to mothership link can be established with 5W over 50km distance with a positive link margin. However, in the distributed scenario, upto 15W is desired to establish a link over 100km, which could be

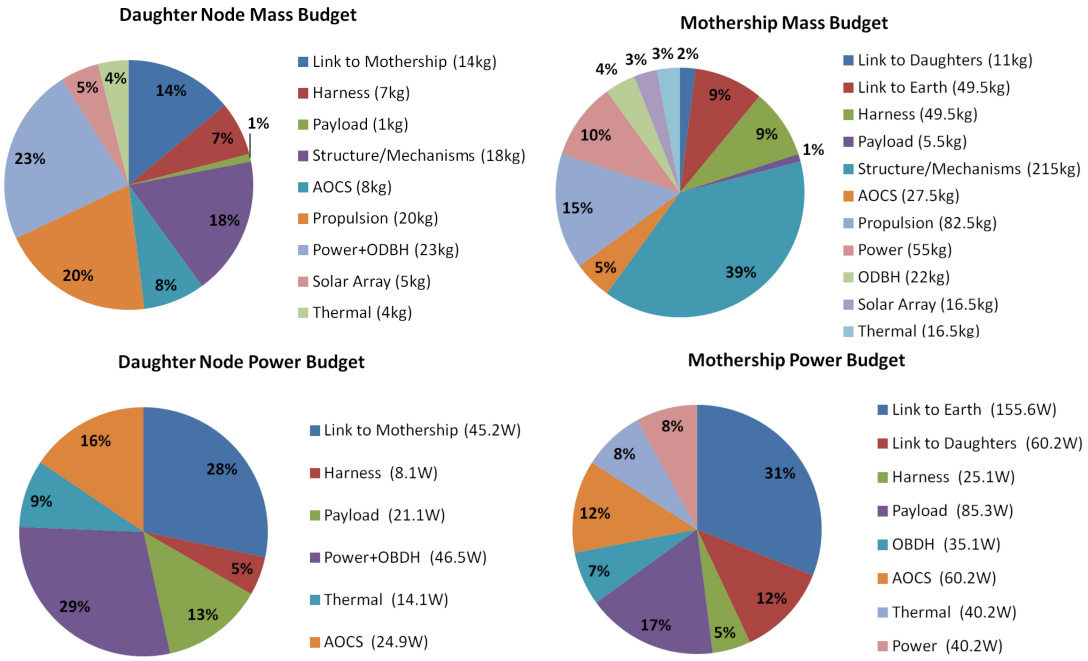

Figure 13: The figure shows the mass and power budget analysis of the DARIS mission.The DARIS study consists of 8 Daughter nodes and 1 centralized mothership. The mass (and power) of each Daughter satellite and mothership was estimated to be 100kg (160W) and 550kg (502W) respectively.

improved using clustering schemes and multi-hop communication (Section 5). Nonetheless, the proposed distributed framework is indispensable for large and scalable array of ≥ 10 satellites, where SPOF must be avoided.

The on-board clock on all satellites must have an Allan-deviation of $\leq 10^{-12}$, which can be met by a Rubidium or OCXO clock (Section 4.3). The current bulky space-qualified clocks, such as Airbus OCXO-F, will potentially be replaced by light-weight and low-power on-chip atomic clocks e.g., the chip-scale SA.45s or Airbus OCXO-H. In inaccessible (e.g., Moon-farside) or far-away deployment scenarios (e.g., Lagrange points), the satellites can be synchronized and localized using MGLS like algorithms, which enable the satellite network to be a co-operative network, with minimum dependence on Earth-based ground stations (Section 6). In addition, the orientation of the satellites can be estimated using the sensors in the attitude and orbit control system (AOCS) which include the sun sensor and star trackers. All satellites will also be equipped with sufficient propulsion to ensure precise deployment and to maintain the maximum baseline separation of 100km (Section 7).

8.1 Technological challenges for ULW arrays

The definitive satellite implementation is intricately connected to specific mission requirements, the number of satellites, the active choices in network architecture and the deployment location. However, recent studies which investigated centralized scenarios for an ULW array give insights into the current state-of-the-art space technology. Figure 13 shows the mass and power breakdown for the DARIS mission, where all subsystems use only available off the shelf components (14). The power consumption for the Daughter satellite and the mothership was estimated at 160W and 502W respectively. Reliable and highly efficient solar panels based on triple junction GaAs cells were employed on both the mothership and Daughter nodes to meet the power re-

quirements. Furthermore, the dry mass of each daughter node was estimated at $\sim$ 100kg and the mothership at $\sim$ 550kg.

In comparison to DARIS, futuristic missions such as OLFAR are expected to be lighter by two orders of magnitude, and consuming an order of magnitude less power (see Table 1). The reduced mass and power requirements will not only enable a larger array of antennas for radio astronomy, but can potentially enable the system to piggy-back on other missions, without the need for a dedicated launch vehicle. To this end, future missions will possibly consist of relatively cheaper nano-satellites with miniaturized and power-efficient subsystems.

The intra-satellite communication between the satellite nodes is a fundamental bottleneck, which limits the bandwidth of observation and possibly the achievable baseline for radio astronomy imaging (see Section 5.2). In addition to limiting the feasibility of the science cases, the power consumption of existing technologies is also high. The DARIS study indicates that over 25% of the energy is spent on communication, for both the Daughter satellite and the mothership (Figure 13). Moreover, one of the limiting factors for the number of satellites is the downlink data rate of the satellite network, such as the HBA XDU for the centralized architecture (see Section 5.3). In case of a distributed architecture, the satellite swarm will employ diversity schemes to cooperatively downlink data to earth (18).

In addition, potential research areas identified during thee studies include the antenna and LNA design for observation frequencies below 10MHz, development of efficient imaging techniques for radio astronomy, high speed and robust RF inter-satellite communications techniques (17), and investigating control and reliability of large satellite arrays (28). In addition, observability challenges such as the unknown RFI environment at the desired deployment location must also be investigated, possibly by a smaller array of satellites via a precursor mission.

8.2 Conclusion

The frequency window of $\leq$ 30 MHz opens a new realm of interesting science cases, and yet remains the last unexplored frequency regime in astronomy. To achieve the science objectives at these wavelengths with the desired resolution and sensitivity, a dedicated space-based ULW array is necessary. Recent advances in technology and computing resources have improved both the feasibility and scientific desirability of such a space-based array. In this article, we justified the need for a space-based antenna array for ultra-long wavelength radio astronomy and discussed various subsystems needed to achieve the desired science cases. More recently concluded projects such as DARIS, FIRST, SURO have shown feasibility of such an array. In particular, the DARIS project showed that a cluster of less than 10 satellites can be launched using current off the shelf technology. An expanded set of science cases can be targeted by up-scaling the number of satellite nodes, extending the frequency range of observation and increasing the instantaneous bandwidth. However, this would significantly increase the mass, power consumption and eventually the cost of the mission. The on-going work on miniaturized nano-satellites may overcome this bottleneck and could pave the way for feasible and affordable missions in the future e.g., OLFAR (59).

Acknowledgments The authors would like to thank all the project members of DARIS, OLFAR and SURO for discussions, in particular Willem Baan, Heino Falcke and Kees van't Klooster. We also thank our reviewers for their insightful comments, which helped improve the quality of the manuscript. This research was funded in part by two projects namely, the STW-OLFAR study (Contract Number: 10556) within the Dutch ASSYS perspectief program and secondly the ESA-funded DARIS Study "Feasibility of Very Large Effective Receiving Antenna Aperture in Space" (Contract Number: 22108/08/NL/ST).

Cite this article as:
Raj Thilak Rajan, Albert-Jan Boonstra, Mark Bentum, Marc Klein-Wolt, Frederik Belien, Michel Arts, Noah Saks, and Alle-Jan van der Veen. "Space-based aperture array for ultra-long wavelength radio astronomy." Experimental Astronomy 41, no. 1-2 (2016): 271-306. https://doi.org/10.1007/s10686-015-9486-6

References

[1] Airbus Defense and Space: Quartz crystal oscillators OCXO-F. Tech. rep., Airbus Defense and Space (2012). URL http://www.space-airbusds.com/en/equipment/quartz-crystal-oscillators-ocxo-f.html. Available online at www.space-airbusds.com/en/equipment/quartz-crystal-oscillators-ocxo-f.ht

[2] Airbus Defense and Space: Quartz crystal oscillators OCXO-H. Tech. rep., Airbus Defense and Space (2015). URL http://www.space-airbusds.com/en/equipment/quartz-crystal-oscillators-ocxo-h.html. Available online at www.space-airbusds.com/en/equipment/quartz-crystal-oscillators-ocxo-h.ht

[3] Alexander, J., Kaiser, M., Novaco, J., Grena, F., Weber, R.: Scientific instrumentation of the Radio-Astronomy-Explorer-2 satellite. NASA STI/Recon Technical Report N **75**, 18284 (1974)

[4] Altunin, V.: Protecting Space-Based Radio Astronomy. In: R.J. Cohen, W.T. Sullivan (eds.) Preserving the Astronomical Sky, *IAU Symposium*, vol. 196, p. 324 (2001)

[5] Aminaei, A., Wolt, M.K., Chen, L., Bronzwaer, T., Pourshaghaghi, H.R., Bentum, M.J., Falcke, H.: Basic radio interferometry for future lunar missions. In: 2014 IEEE Aerospace Conference, pp. 1–19. IEEE (2014)

[6] Arts, M., van der Wal, E., Boonstra, A.J.: Antenna concepts for a space-based low-frequency radio telescope. In: ESA Antenna Workshop on Antennas for Space Applications, Noordwijk, pp. 5–8 (2010)

[7] Baan, W.: SURO-LC: A space-based ultra-long wavelength radio observatory. In: Proceedings of the meeting 'From Antikythera to the Square Kilometre Array: Lessons from the Ancients' (Antikythera & SKA). 12-15 June 2012. Kerastari, Greece., vol. 1, p. 45 (2012)

[8] Barnes, J.A., Chi, A.R., Cutler, L.S., Healey, D.J., Leeson, D.B., McGunigal, T.E., Mullen, J.A., Smith, W.L., Sydnor, R.L., Vessot, R.F.C., Winkler, G.M.R.: Characterization of

frequency stability. IEEE Transactions on Instrumentation and Measurement **IM-20**(2), 105 –120 (1971)

[9] Basart, J., Burns, J., Dennison, B., Weiler, K., Kassim, N., Castillo, S., McCune, B.: Directions for space-based low frequency radio astronomy: 1. System considerations. Radio Science **32**(1), 251–263 (1997)

[10] Basart, J., Burns, J., Dennison, B., Weiler, K., Kassim, N., Castillo, S., McCune, B.: Directions for space-based low-frequency radio astronomy: 2. Telescopes. Radio Science **32**(1), 265–275 (1997)

[11] Bentum, M., Verhoeven, C., Boonstra, A.J., van der Veen, A.J., Gill, E.: A novel astronomical application for formation flying small satellites. In: 60th International Astronautical Congress: IAC 2009, 12-16 October 2009, Daejeon, Republic of Korea (2009). Available online at http://doc.utwente.nl/68514

[12] Bergman, J.E.S., Blott, R.J., Forbes, A.B., Humphreys, D.A., Robinson, D.W., Stavrinidis, C.: FIRST Explorer – An innovative low-cost passive formation-flying system. arXiv (2009). URL http://adsabs.harvard.edu/abs/2009arXiv0911.0991B. Available online at http://arxiv.org/abs/0911.0991

[13] Bik, J., Visser, P., Jennrich, O.: LISA satellite formation control. Advances in Space Research **40**(1), 25–34 (2007)

[14] Boonstra, A.J., Bentum, M., Rajan, R.T., Wijnholds, S.J., van Cappellen, W., Saks, N., Falcke, H., Klein-Wolt, M.: DARIS: Distributed aperture array for radio astronomy in space. Tech. Rep. 08, ASTRON, Dwingeloo (2011)

[15] Boonstra, A.J., Saks, N., Bentum, M., van't Klooster, K., Falcke, H.: DARIS, A low-frequency distributed aperture array for radio astronomy in space. In: 61st International Astronautical Congress. IAC, IAC (2010)

[16] Borg, I., Groenen, P.J.F.: Modern Multidimensional Scaling: Theory and Applications (Springer Series in Statistics), 2nd edn. Springer (2005)

[17] Budianu, A., Castro, T.J.W., Meijerink, A., Bentum, M.: Inter-satellite links for cubesats. In: IEEE Aerospace Conference, pp. 1–10 (2013). DOI 10.1109/AERO.2013.6496947

[18] Budianu, A., Meijerink, A., Bentum, M.: Swarm-to-earth communication in {OLFAR}. Acta Astronautica **107**(0), 14 – 19 (2015). DOI http://dx.doi.org/10.1016/j.actaastro.2014.10.041. URL http://www.sciencedirect.com/science/article/pii/S0094576514004196

[19] Budianu, A., Rajan, R.T., Engelen, S., Meijerink, A., Verhoeven, C., Bentum, M.: OLFAR: Adaptive topology for satellite swarms. In: International Astronautical Congress, Cape Town, pp. 3–7 (2011)

[20] Bunton, J.: SKA correlator advances. Experimental Astronomy **17**, 251–259 (2004). DOI 10.1007/s10686-005-5661-5

[21] Burke, B.F.: Astrophysics from the moon. Science **250**(4986), 1365–1370 (1990)

[22] Burns, J.: The lunar observer radio astronomy experiment (LORAE). Low frequency astrophysics from space pp. 19–28 (1990)

[23] Burns, J.O., Duric, N., Taylor, G.J., Johnson, S.W.: Observatories on the moon. Scientific American **262**, 42–49 (1990)

[24] Burns, J.O., Lazio, J., Bale, S., Bowman, J., Bradley, R., Carilli, C., Furlanetto, S., Harker, G., Loeb, A., Pritchard, J.: Probing the first stars and black holes in the early universe with the dark ages radio explorer (DARE). Advances in Space Research **49**(3), 433–450 (2012)

[25] Cohen, A.: Estimates of the classical confusion limit for the LWA. Long Wavelength Array Memo Series 17, Naval Research Laboratory, Washington, DC 20375 (2004). URL http://www.ece.vt.edu/swe/lwa/memo/lwa0017.pdf

[26] Droz, F., Barmaverain, G., Wang, Q., Rochat, P., Emma, F., Waller, P.: Galileo rubidium standard - lifetime data and GIOVE-A related telemetries. In: 21st European Frequency and Time Forum, pp. 1122–1126. IEEE (2007)

[27] Ellingson, S.W., Clarke, T.E., Cohen, A., Craig, J., Kassim, N.E., Pihlstrom, Y., Rickard, L.J., Taylor, G.B.: The long wavelength array. Proceedings of the IEEE **97**(8), 1421–1430 (2009)

[28] Engelen, S., Gill, E., Verhoeven, C.: On the reliability, availability, and throughput of satellite swarms. IEEE Transactions on Aerospace and Electronic Systems **50**(2), 1027–1037 (2014). DOI 10.1109/TAES.2014.120711

[29] Gorgolewski, S.: The advantages of a lunar radio astronomy observatory. Astronautica Acta, New Series **11**(2), 130–131 (1965)

[30] Goujon, D., Rochat, P., Mosset, P., Boving, D., Perri, A., Rochat, J., Ramanan, N., Simonet, D., Vernez, X., Froidevaux, S., et al.: Development of the space active hydrogen maser for the aces mission. In: EFTF-2010 24th European Frequency and Time Forum, pp. 1–6. IEEE (2010)

[31] Gurvits, L.: Space radio astronomy in the next 1000001 (binary) years. In: Resolving The Sky-Radio Interferometry: Past, Present and Future, vol. 1, p. 45 (2012)

[32] Hirabayashi, H., Hirosawa, H., Kobayashi, H., Murata, Y., Asaki, Y., Avruch, I.M., Edwards, P.G., Fomalont, E.B., Ichikawa, T., Kii, T., et al.: The VLBI space observatory programme and the radio-astronomical satellite halca. Publications of the Astronomical Society of Japan **52**(6), 955–965 (2000)

[33] IEEE 2007: Part 15.4: Wireless medium access control (MAC) and physical layer (PHY) specifications for low-rate wireless personal area networks (WPANs). Tech. rep., IEEE Working Group 802.15.4 (2007)

[34] Jester, S., Falcke, H.: Science with a lunar low-frequency array: From the dark ages of the Universe to nearby exoplanets. New Astronomy Reviews **53**, 1–26 (2009). DOI 10.1016/j.newar.2009.02.001

[35] Jones, D., Allen, R., Basart, J., Bastian, T., Blume, W., Bougeret, J.L., Dennison, B., Desch, M., Dwarakanath, K., Erickson, W., et al.: The alfa medium explorer mission. Advances in Space Research **26**(4), 743–746 (2000)

[36] Jones, D.L., Lazio, J., MacDowall, R., Weiler, K., Burns, J.: Towards a lunar epoch of reionization telescope. In: Bulletin of the American Astronomical Society, vol. 39, p. 196 (2007)

[37] Kaiser, M.L., Weiler, K.W.: The Current Status of Low Frequency Radio Astronomy from Space. Geophysical monograph **119**, 1–11 (2000). URL http://adsabs.harvard.edu/abs/2000ralw.conf....1K

[38] Kardashev, N., Khartov, V., Abramov, V., Avdeev, V.Y., Alakoz, A., Aleksandrov, Y.A., Ananthakrishnan, S., Andreyanov, V., Andrianov, A., Antonov, N., et al.: "RadioAstron"-a telescope with a size of 300 000 km: Main parameters and first observational results. Astronomy Reports **57**(3), 153–194 (2013)

[39] Kassim, N.E., Perley, R.A., Erickson, W.C., Dwarakanath, K.S.: Subarcminute resolution imaging of radio sources at 74 MHz with the Very Large Array. The Astronomical Journal **106**, 2218–2228 (1993). DOI 10.1086/116795

[40] Kay, S.M.: Fundamentals of statistical signal processing: estimation theory. Prentice-Hall, Inc., Upper Saddle River, NJ, USA (1993)

[41] Klein-Wolt, M., Aminaei, A., Zarka, P., Schrader, J.R., Boonstra, A.J., Falcke, H.: Radio astronomy with the european lunar lander: Opening up the last unexplored frequency regime. Planetary and Space Science **74**(1), 167 – 178 (2012). DOI http://dx.doi.org/10.1016/j.pss.2012.09.004. URL http://www.sciencedirect.com/science/article/pii/S0032063312002796. Scientific Preparations For Lunar Exploration

[42] Klein-Wolt M. et al.: Dark ages explorer, DEX, a white paper for a low frequency radio interferometer mission to explore the cosmological dark ages for the L2 (2013). URL https://astro.ru.nl/wiki/_media/research/dex/dex_whitepaper.pdf. L3 ESA Cosmic Vision Program

[43] Kuiper, T., Jones, D.: Lunar surface arrays. Radio Astronomy at Long Wavelengths pp. 351–357 (2000)

[44] Linfield, R., Keihm, S., Teitelbaum, L., Walter, S., Mahoney, M., Treuhaft, R., Skjerve, L.: A test of water vapor radiometer-based troposphere calibration using very long baseline interferometry observations on a 21-km baseline. Radio Science **31**(1), 129–146 (1996)

[45] Loeb, A., Zaldarriaga, M.: Measuring the small-scale power spectrum of cosmic density fluctuations through 21 cm tomography prior to the epoch of structure formation. Physical Review Letters **92**(21), 211301 (2004)

[46] Lombardi, M.A., Nelson, L.M., Novick, A.N., Zhang, V.S.: Time and frequency measurements using the global positioning system. Cal Lab: International Journal of Metrology **8**(3), 26–33 (2001)

[47] Lonsdale, C., et al.: The murchison widefield array: Design overview. Proceedings of the IEEE **97**(8), 1497–1506 (2009). DOI 10.1109/JPROC.2009.2017564

[48] Maccone, C.: NASA gateways at L1 and L2 and the radio-quiet moon farside imperative. Acta Astronautica **57**(2â€“8), 145 – 155 (2005). DOI http://dx.doi.org/10.1016/j.actaastro.2005.02.005. URL http://www.sciencedirect.com/science/article/pii/S0094576505000597. Selected Proceedings of the 55th International Astronautical Federation Congress, Vancouver, Canada, 4-8 October 2004

[49] Manning, R.: Instrumentation for space-based low frequency radio astronomy. Geophysical Monograph Series **119**, 329–337 (2000)

[50] Markley, F.L., Crassidis, J.L.: Fundamentals of Spacecraft Attitude Determination and Control, vol. 33. Springer (2014)

[51] Microsemi: SA.45sCSAC- Chip Scale Atomic Clock datasheet. Tech. rep., Microsemi (2011). Available online at www.microsemi.com/products/timing-synchronization-systems/embedded-timing-solutions/com

[52] Naghshvar, M., Zhuang, H., Javidi, T.: A general class of throughput optimal routing policies in multi-hop wireless networks. IEEE Transactions on Information Theory **58**(4), 2175–2193 (2012)

[53] Nee, R.v., Prasad, R.: OFDM for wireless multimedia communications. Artech House, Inc. (2000)

[54] Oberoi, D., Pinçon, J.L.: A new design for a very low frequency spaceborne radio interferometer. Radio science **40**(4) (2005)

[55] Patwari, N., Ash, J., Kyperountas, S., Hero A.O., I., Moses, R., Correal, N.: Locating the nodes: Cooperative localization in wireless sensor networks. IEEE Signal Processing Magazine **22**(4), 54 – 69 (2005). DOI 10.1109/MSP.2005.1458287

[56] Quillien, K., Engelen, S., Gill, E., Smith, D., Arts, M., Boonsta, A.J.: Astronomical antenna for a space based low frequency radio telescope. In: 27th Conference on Small Satellites, pp. 1–4 (2013)

[57] Rajan, R.T., Bentum, M., Boonstra, A.J.: Synchronization for space based ultra low frequency interferometry. In: IEEE Aerospace Conference, pp. 1–8 (2013)

[58] Rajan, R.T., Bentum, M., Gunst, A., Boonstra, A.J.: Distributed correlators for interferometry in space. In: IEEE Aerospace Conference, pp. 1–9 (2013)

[59] Rajan, R.T., Engelen, S., Bentum, M., Verhoeven, C.: Orbiting Low Frequency Array for Radio astronomy. In: IEEE Aerospace Conference, pp. 1 –11 (2011)

[60] Rajan, R.T., Leus, G., van der Veen, A.J.: Joint relative position and velocity estimation for an anchorless network of mobile nodes. Signal Processing **115**(0), 66 – 78 (2015). DOI http://dx.doi.org/10.1016/j.sigpro.2015.02.023. URL http://www.sciencedirect.com/science/article/pii/S0165168415000894

[61] Rajan, R.T., van der Veen, A.J.: Joint ranging and synchronization for an anchorless network of mobile nodes. IEEE Transactions on Signal Processing, **63**(8), 1925–1940 (2015). DOI 10.1109/TSP.2015.2391076

[62] Rees, M.J.: The End of the 'Dark Age'. In: S. Holt, E. Smith (eds.) After the Dark Ages: When Galaxies were Young (the Universe at $2 < z < 5$), *American Institute of Physics Conference Series*, vol. 470, pp. 13–23. AIP Publishing (1999)

[63] Saks, N., Boonstra, A.J., Rajan, R.T., Bentum, M.J., Beilen, F., van't Klooster, K.: DARIS, a fleet of passive formation flying small satellites for low frequency radio astronomy. In: The 4S Symposium (Small Satellites Systems & Services Symposium), Madeira, Portugal, 31 May - 4 June 2010 (ESA and CNES conference) (2010)

[64] Serpedin, E., Chaudhari, Q.M.: Synchronization in Wireless Sensor Networks: Parameter Estimation, Peformance Benchmarks, and Protocols, 1st edn. Cambridge University Press, New York, NY, USA (2009)

[65] Smith, D., Arts, M.: Characterization of astronomical antenna for space based low frequency radio telescope. In: IEEE Aerospace Conference, March 2-9, 2013, Big Sky, Montana US (2013)

[66] Smith, H.J.: Very low frequency radio astronomy from the moon. In: Low Frequency Astrophysics from Space, pp. 29–33. Springer (1990)

[67] Sodnik, Z., Furch, B., Lutz, H.: Free-space laser communication activities in Europe: SILEX and beyond. In: 19th Annual Meeting of the IEEE Lasers and Electro-Optics Society (LEOS), pp. 78–79 (2006). DOI 10.1109/LEOS.2006.278845

[68] Stanford: PRS10-rubidium frequency standard. Tech. rep., Stanford (2006). URL http://www.leapsecond.com/museum/prs10/. Available online at www.leapsecond.com/museum/prs10/

[69] Takahashi, Y.D.: A concept for a simple radio observatory at the lunar south pole. Advances in Space Research **31**(11), 2473–2478 (2003)

[70] Taylor, G.B., Carilli, C.L., Perley, R.A. (eds.): Synthesis Imaging in Radio Astronomy II, *Astronomical Society of the Pacific Conference Series*, vol. 180. Astronomical Society of the Pacific, San Francisco (1999)

[71] Thompson, A.R., Moran, J.M., Swenson Jr, G.W.: Interferometry and synthesis in radio astronomy. John Wiley & Sons (2008)

[72] Toyoshima, M.: Trends in satellite communications and the role of optical free-space communications. Journal of Optical Networking **4**(6), 300–311 (2005). DOI 10.1364/JON.4.000300. URL http://jon.osa.org/abstract.cfm?URI=jon-4-6-300

[73] Ulvestad, J.S., Edwards, C.D., Linfield, R.P.: Very long baseline interferometry using a radio telescope in earth orbit. Tech. Rep. 42-88, JPL (1986)

[74] van Haarlem, M.P., et al.: LOFAR: The LOw-Frequency ARray. Astronomy & Astrophysics **556**, A2 (2013). DOI 10.1051/0004-6361/201220873

[75] Weber, R., Alexander, J., Stone, R.: The radio astronomy explorer satellite, a low-frequency observatory. Radio Science **6**(12), 1085–1097 (1971)

[76] Weiler, K., Johnston, K., Simon, R., Dennison, B., Erickson, W., Kaiser, M., Cane, H., Desch, M.: A low frequency radio array for space. Astronomy and Astrophysics **195**, 372–379 (1988)

[77] Wijnholds, S.J., van der Tol, S., Nijboer, R., van der Veen, A.J.: Calibration challenges for future radio telescopes. IEEE Signal Processing Magazine **27**(1), 30–42 (2010)

[78] Woan, G.: A very low frequency radio telescope on the far side of the moon. In: Measuring the Size of Things in the Universe: HBT Interferometry and Heavy Ion Physics, vol. 1, p. 347 (1999)

[79] Zarka, P., Bougeret, J.L., Briand, C., Cecconi, B., Falcke, H., Girard, J., GrieÃŸmeier, J.M., Hess, S., Klein-Wolt, M., Konovalenko, A., Lamy, L., Mimoun, D., Aminaei, A.: Planetary and exoplanetary low frequency radio observations from the moon. Planetary and Space Science **74**(1), 156–166 (2012). DOI http://dx.doi.org/10.1016/j.pss.2012.08.004. URL http://www.sciencedirect.com/science/article/pii/S0032063312002413. Scientific Preparations For Lunar Exploration